Trends and Uncertainties of Regional Barystatic Sea-level Change in the Satellite Altimetry Era

Carolina M.L. Camargo[1,2], Riccardo E.M. Riva[2], Tim H.J. Hermans[1,2], and Aimée B.A. Slangen[1]

[1]NIOZ Royal Netherlands Institute for Sea Research, Department of Estuarine and Delta Systems, Yerseke, the Netherlands
[2]Delft University of Technology, Department of Geoscience and Remote Sensing, Delft, the Netherlands

Correspondence: Carolina M.L. Camargo (carolina.camargo@nioz.nl)

Abstract.

Ocean mass change is one of the main drivers of present-day sea-level change (SLC). Also known as barystatic SLC, it is driven by the exchange of freshwater between the land and the ocean, such as melting of continental ice from glaciers and ice sheets, and variations in land water storage. While many studies have quantified the present-day barystatic contribution to
5 global mean SLC, fewer works have looked into regional changes. This study provides a comprehensive analysis of regional barystatic SLC trends since 1993 (the satellite altimetry era), with a focus on the uncertainty budget. We consider three types of uncertainties: intrinsic (the uncertainty from the data/model itself); temporal (related to the temporal variability in the time series); and spatial-structural (related to the location/distribution of the mass change sources). We collect a range of estimates for the individual freshwater sources, which are used to compute regional patterns (fingerprints) of barystatic SLC
10 and analyse the different types of uncertainty. When all the contributions are combined, we find that the barystatic sea-level trends regionally ranges from -0.43 to 2.55 mm.year^{-1} for 2003-2016, and from -0.39 to 2.00 mm.year^{-1} for 1993-2016, depending on the choice of dataset. When all types of uncertainties from all contributions are combined, the total barystatic uncertainties regionally range from 0.62 to 1.29 mm.year^{-1} for 2003-2016, and from 0.35 to 0.90 mm.year^{-1} for 1993-2016, also depending on the dataset choice. We find that the temporal uncertainty dominates the budget, although the spatial-structural
15 also has a significant contribution. On average, the intrinsic uncertainty plays a small part in the uncertainty budget. The main source of uncertainty is the temporal uncertainty from the land water storage contribution, which is responsible for at least 50% of the total uncertainty, depending on the region of interest. The second main contributions come from the spatial-structural uncertainty from Antarctica and land water storage, which show that different locations of mass change can lead to trend deviations larger than 20%. As the barystatic SLC contribution and its uncertainty vary significantly from region to region,
20 better insights into regional SLC are important for local management and adaptation planning.

Plain Language Summary

The ice melt from Antarctica, Greenland and glaciers, and variations in land water storage cause sea-level changes. Here, we characterise the regional trends within these sea-level changes, taking into account mass variations since 1993. We take a

holistic approach for determining the uncertainties of these sea-level changes, considering different types of errors. Our study
25 reveals the importance of clearly quantifying the uncertainties of sea-level change estimates.

Keywords

Ocean Mass; Sea-level change; Sea-level equation; Ice sheets; Glaciers; Land Water Storage

1 Introduction

Even if all countries keep to the Paris Agreement, global mean sea level will continue to rise in the coming decades and beyond
30 (Wigley, 2005; Nicholls et al., 2007; Oppenheimer et al., 2019; Fox-Kemper et al., 2021). The reason for this is the long
response time of the ocean and the cryosphere to climate change (Abram et al., 2019). As a consequence societies all over
the world will need to deal with a certain amount of sea-level change (SLC). Therefore, a good understanding of present day
SLC and its drivers is required, as it yields better future sea-level projections, which are necessary for adaption and mitigation
planning.
35   The attribution of SLC to its different drivers is known as the sea-level budget (WCRP, 2018). Alongside density driven
(steric) changes (e.g., MacIntosh et al. (2017); Camargo et al. (2020)), present day SLC is mainly driven by the mass loss of
continental ice stored in glaciers and ice sheets, and by variations in land water storage (LWS) (WCRP, 2018; Fox-Kemper
et al., 2021). The contribution of ocean mass changes, known as barystatic SLC (Gregory et al., 2019), was responsible for
about 60% of the global mean SLC over the 20th century (Frederikse et al., 2020; Fox-Kemper et al., 2021). Barystatic SLC
40 has a characteristic regional pattern, varying significantly from region to region and strongly depending on the location of mass
loss (Mitrovica et al., 2001). For example, a collapse of the West Antarctic Ice Sheet would cause sea level to rise 1.6 times
more in San Francisco (US) than in Santiago (Chile) (Gomez et al., 2010). Thus, for local management and climate planning,
it is important to understand the barystatic contribution to regional SLC (Larour et al., 2017).
        Regional barystatic SLC estimates can be computed by solving the sea-level equation (SLE) (Farrell and Clark, 1976),
45 which results in the so-called sea-level fingerprints (Mitrovica et al., 2001). Fingerprints of barystatic SLC have been the
subject of several studies, ranging from investigating the effects of variations in paleoclimate, for example the SLC due to the
last deglaciation event (Lin et al., 2021), to contemporary SLC (Frederikse et al., 2020). Most of the studies including present-
day barystatic SLC have focused either on the GRACE satellite period (since 2002) (Bamber and Riva, 2010; Riva et al., 2010;
Hsu and Velicogna, 2017; Adhikari et al., 2019; Frederikse et al., 2019), on the closure of the sea-level budget over a longer
50 period (Slangen et al., 2014; Frederikse et al., 2020) or on the barystatic contribution to global mean SLC (Chambers et al.,
2007; Horwath et al., 2021). However, an in-depth analysis of regional barystatic SLC and its uncertainties during the satellite
altimetry era (since 1993) has not yet been done. Insights into the contributions of ice sheets, glaciers and land water storage
to regional SLC and their uncertainties over the last three decades are important to constrain regional sea-level projections and
obtain a better closure of the regional sea-level budget.

55   The importance of quantifying the uncertainties in sea-level studies has increasingly received attention (Bos et al., 2014; Royston et al., 2018; Ablain et al., 2019; Camargo et al., 2020; Palmer et al., 2021; Prandi et al., 2021; Horwath et al., 2021). One of the approaches to describe the uncertainties of a system is to partition the total uncertainty budget into different kinds of uncertainties. Errors in the measurement system, known as intrinsic uncertainties (Palmer et al., 2021), describe the sensitivities of choices within a methodology (Thorne, 2021). The intrinsic uncertainties, also referred as observational (Ablain

60   et al., 2019; Prandi et al., 2021) or parametric (Thorne, 2021), need to be determined during the low-level data processing and are usually provided with higher level (ready-to-use) products. Another class of uncertainties originates from the use of different methodologies to describe the same physical system, known as structural uncertainty (Thorne et al., 2005; Palmer et al., 2021). This can be defined as the spread around a central (ensemble) estimate. The structural uncertainty is related to the use of different datasets of the same process. For regional barystatic SLC, the spread in the location of the mass loss introduces

65   another source of error, which we call spatial uncertainty. Finally, another type of uncertainty results from the autocorrelation of the observations (Bos et al., 2013), which we refer to as temporal uncertainty. This uncertainty becomes relevant when a functional model, such as a (linear) trend, is used to describe the changes within the system. The temporal uncertainty can be estimated by using noise models while determining the trend. Together, the intrinsic, structural, spatial and temporal uncertainties describe the uncertainties of an observed quantity, in this case the regional barystatic SLC.

70   The aim of this work is to provide a comprehensive overview of regional barystatic SLC with a focus on the global and regional uncertainty budget. To do so, we use state-of-the-art datasets of mass contributions from land ice and LWS (Section 2.1) to compute regional sea-level fingerprints (Section 2.2.1). In addition, we present a methodological framework to describe the uncertainties of the fingerprints (Section 2.2.2). We follow the noise model analysis of Camargo et al. (2020) to quantify the *temporal uncertainty* (Section 3.1;3.2). We combine the effect of ice geometry on sea-level fingerprints (Bamber and Riva,

75   2010; Mitrovica et al., 2011) with the structural uncertainty definition of Palmer et al. (2021), to compute the *spatial-structural uncertainty* of the fingerprints (Section 3.3). Together with the *intrinsic uncertainty* (Section 3.4), we present the total barystatic trend and uncertainty for 2003-2016 and 1993-2016 (Section 3.5). We finalize this manuscript with an overview and discussion of our findings (Section 4).

2   Data and Methodology

80   ### 2.1   Datasets

We use estimates of the contributions of mass changes of the Antarctic and Greenland ice sheets (AIS and GIS, respectively), glaciers (GLA), and land water storage (LWS). We define LWS anomalies as water mass changes outside glacierized areas: the sum of water stored in rivers, lakes, wetlands, artificial reservoirs, snow pack, canopy and soil (groundwater) (Cáceres et al., 2020). For each of the barystatic contributions we use four different estimates (Table 1, and discuss in more detail in

85   Supplementary Text A).

One of the main sources of observations of Earth's mass changes is the satellite mission Gravity Recovery and Climate Experiment (GRACE,Tapley et al. (2004)) and its follow-on mission (GRACE-FO, Landerer et al. (2020)). We use GRACE

mass concentrations (mascons) over land as estimates of changes in AIS, GIS, glaciers and LWS. To avoid methodological biases, we use mascon solutions from two different processing centers: RL06 from Center for Spatial Resarch (CSR) (Save et al., 2016; Save, 2020) and RL06 v02 from Jet Propulsion Laboratory (JPL) (Watkins et al., 2015; Wiese et al., 2019) (Table 1). To isolate the individual contributions of AIS, GIS, LWS and GLA in the GRACE mascons, we use an ocean-land-cryosphere mask, which delineates the drainage basins of the ice sheets (based on Mouginot and Rignot (2019),Rignot et al. (2011), the glaciers (based on the Randolph Glacier Inventory, Consortium (2017)), and the remaining land regions (based on ETOPO1, Amante and Eakins (2009)).

Apart from GRACE data, which is only available since late 2002, we use seven other datasets in our analysis, from which five are independent of GRACE and two are partly based on GRACE (Table 1). For LWS, we use data from two global hydrological models: PCR-GLOBWB (GWB, Sutanudjaja et al. (2018)) and WaterGAP (WGP, Cáceres et al. (2020)). The latter also incorporates a time series of glacier mass variations from the global glacier model of Marzeion et al. (2012). We use our ocean-land-cryosphere mask to separate the LWS and GLA estimated from WGP. For GLA, in addition to the WGP model simulations, we also use observational estimates from Zemp et al. (2019), which are based on an extrapolation of glaciological and geodetic observations. For the GIS and AIS, we use observation- and model-based data from Mouginot et al. (2019) and Rignot et al. (2019), respectively. We refer to these as UCI datasets, since they were both developed at the University of California at Irvine (UCI). We also use AIS and GIS estimates from the ice sheet mass balance inter-comparison exercise (IMBIE, Shepherd et al. (2018, 2020)), which combines ice sheet mass balance estimates developed from three different techniques (satellite altimetry, satellite gravimetry and the input-output method). Since the IMBIE datasets incorporate both GRACE observations and UCI datasets, thus we define them as a *hybrid* datasets in Table 1.

Table 1. Overview of datasets used in this manuscript.

Contribution	Dataset	Temporal range	Source	Dependence on GRACE	Acronym
All	CSR mascon RL06	2003-2020	observations	GRACE(-FO)	CSR
	JPL mascon RL06	2003-2020	observations	GRACE(-FO)	JPL
AIS	IMBIE 2018	1993-2016	ensemble datasets	Hybrid	IMB
	Rignot 2019	1979-2017	observations + model	Independent	UCI
GIS	IMBIE 2020	1993-2018	ensemble datasets	Hybrid	IMB
	Mouginot 2019	1972-2018	observations + model	Independent	UCI
Glaciers	Zemp 2019	1962-2016	observations + model	Independent	ZMP
	WaterGAP	1958-2016	glaciers model	Independent	WGP
LWS	WaterGAP	1958-2016	hydrological model	Independent	WGP
	PCR-GLOBWB	1948-2016	hydrological model	Independent	GWB

2.2 Methodological Framework

We characterize barystatic SLC by a linear trend and the three types of uncertainties discussed earlier. We use the following time periods for the trend analysis: from 1993-2016 for the non-GRACE datasets, and from 2003-2016, for all datasets. The framework used to compute and combine the uncertainties and associated regional sea-level patterns is schematized in Figure 1. The main modules of the framework (bold text in the blue boxes of Figure 1a) are further explained in Figure 1b and in sections 2.2.1 and 2.2.2.

The trends and associated temporal uncertainties are estimated directly from the mass source time series (Table 1) in the *noise model* module (Figure 1a), such that the noise model analysis (Section 3.1) describes the physical processes of the mass sources, instead of the temporal correlation in the sea-level fingerprint. The mass source change trend and temporal uncertainty are then used as input to the *SLE model* module (Section 2.2.1), which computes how the mass changes on land affect regional ocean mass change (i.e., barystatic SLC; Section 3.2). The mass source trends are also used as input to the *spatial uncertainty* analysis (Section 3.3). To compute the *intrinsic uncertainty* we start with the uncertainty time series of the source data, as provided with the estimates. We then compute the linear trend arising from an ordinary least squares (OLS) regression. This trend, representing the data uncertainty over land, is used as input to the SLE model, resulting in regional patterns of the *intrinsic uncertainty* of ocean mass sea-level change.

2.2.1 The Sea-Level Equation Model

The regional patterns resulting from the barystatic contributions can be computed by solving the sea-level equation (SLE) (Farrell and Clark, 1976), using spatial and temporal information of GLA, AIS, GIS and LWS (Tamisiea and Mitrovica, 2011) (Figure 1b, left column). Before computing the regional SLC fields, all input data (Table 1) is converted to equivalent water height, and bilinearly interpolated to a 1° by 1° grid. The SLE model then computes how the source mass change is redistributed over the oceans, taking into account the gravitational, deformation and rotational response of the Earth to these mass changes (Milne and Mitrovica, 1998; Mitrovica et al., 2001; Tamisiea and Mitrovica, 2011). The SLE model uses a pseudospectral approach (Mitrovica and Peltier, 1991) up to spherical harmonic degree and order 180 (equivalent to a spatial resolution of one degree). We assume a purely elastic solid-Earth response to the mass redistribution, based on the Preliminary Reference Earth Model (Dziewonski and Anderson, 1981). The model computes relative SLC, which is the difference in height between the geoid and the solid Earth surface.

2.2.2 Trend and Uncertainty Assessment

As described above, we use a linear trend to compute the barystatic SLC, and we define three independent uncertainties (temporal, intrinsic and spatial-structural) to compute the uncertainty budget. Our trends and associated temporal uncertainty (Figure 1b, centre column) are computed using the software Hector (Bos et al., 2013), in which the observations are assumed to be the sum of a deterministic model (including annual and semi-annual signals) and stochastic noise. Different noise models
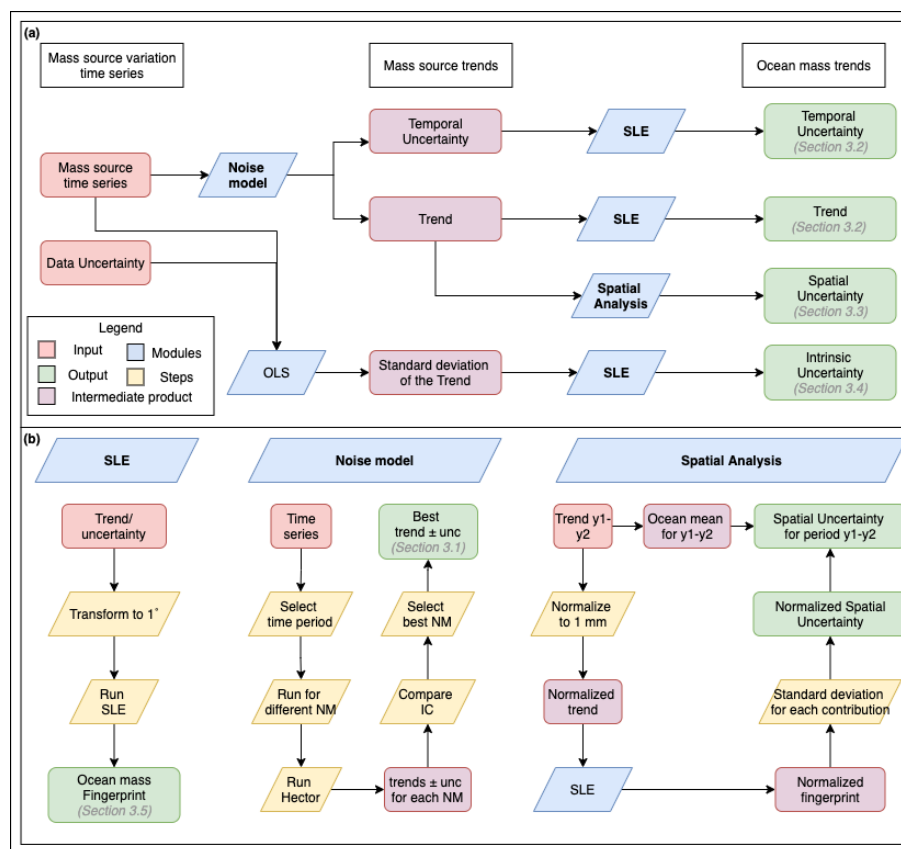
Figure 1. Overview of the framework used in this study (a), with detailed modules (b). Red boxes indicate the initial data (Table 1), purple the intermediate products, and green the final products. The yellow boxes indicate steps of the methodology, and the blue the main modules. We use the following acronyms and abbreviations: OLS: ordinary least-squares; SLE; Sea-level equation; IC: Information Criteria; unc: uncertainty; NM: noise model; Hector: software package by Bos et al. (2013).

can be selected to describe the autocorrelation between the residuals of the regression. The uncertainty of the regression model, representing one standard deviation, is then used as our temporal uncertainty.

140   Based on previous studies (Bos et al., 2013; Royston et al., 2018; Camargo et al., 2020), we test eight noise models to find the best descriptor of the uncertainties in our data:

– white noise (WN), in which no autocorrelation between the residuals is considered;

– pure power law (PL), where all observations influence one another, although their correlation decreases with increasing temporal distance;

145   – PL combined with WN (PLWN);

- – auto-regressive of orders 1, 5, and 9 (AR(1), AR(5), and AR(9), respectively), in which the order represents the number of previous observations influencing the next one;

- – autoregressive fractionally integrated moving average of order 1 (ARF), which combines an AR(1) model with a fractional integration and a moving average of the noise;

150 – generalized Gauss-Markov (GGM), a generalized form of the ARF model.

The goodness of the fit of the models is assessed with the modified Bayesian Information Criterion (BIC_{tp}; He et al. (2019)), which is an intermediate criterion in relation to the Akaike (AIC; Akaike (1974)) and Bayesian (BIC;Schwarz (1978)) criteria. The best noise model is chosen by minimizing the criterion.

The second uncertainty we consider is the spatial-structural uncertainty (Figure 1b, right column). Studies that combine
155 a large number of datasets often base the structural uncertainty of an estimate on the standard deviation over the individual datasets in relation to the ensemble mean (Palmer et al., 2021; Cazenave et al., 2018). However, the small number of samples in our study (4 estimates for each contribution) could lead to unrealistic structural uncertainties when simply based on the standard deviation, as individual outliers could bias the ensemble mean. Instead, we compute the spatial-structural uncertainty by estimating the standard deviation based on the normalized fingerprint for each contribution. First, we use the trend of each
160 contribution to compute sea-level fingerprints normalized to $1 \, \mathrm{mm.year}^{-1}$ of global mean SLC. By doing so, we reduce the effect of outliers on the standard deviation of the fingerprints, and only preserve the effect that the mass source distribution has on the fingerprint shape. We then take the standard deviation across the four datasets for each mass source contribution, which leads to four normalized spatial-structural uncertainties reflecting the uncertainty associated with the different spatial resolutions of the datasets. For example, the spatial-structural uncertainty for AIS, will reflect the differences in the fingerprints
165 due to the fact that GRACE datasets provide observations in a 0.25 degrees resolution, while R19 provides mass changes averaged over the 17 main drainage basins of the ice sheet, and IMB mass changes avergae over the three regions of the ice sheet (west, east and peninsula). While the analysis is based on the 2003-2016 trend, we assume that the normalized fingerprints are time-invariant, and that the resulting uncertainty is also representative of the 1993-2016 period. Lastly, we multiply the normalized uncertainty by the ocean mean central estimate of each contribution for 1993-2016 and 2003-2016 to
170 compute the spatial-structural uncertainty for the respective period. We note that all components show some decadal variability in the spatial distribution, and thus assuming that the spatial mass change distributions from 2003-2016 are representative of the period 1993-2016 is an approximation of the study. However, by multiplying the normalized fingerprint by the mean of each period the possible error from this assumption becomes fairly limited. Furthermore, using a shorter spatially dense time series to obtain the variability of a longer period when only limited information is available is a methodology that is often used
175 in sea-level studies, for example the EOF analysis of Church and White (2006), and the use of GRACE fingerprints to obtain the 20st century barystatic patterns from Frederikse et al. (2020).

The final type of uncertainty considered in our assessment is the intrinsic uncertainty, which represents the formal errors and sensitivities in the measurement system and needs to be provided with the observations/models by the data processor/distribution center. The intrinsic uncertainty was only provided with the JPL and IMBIE datasets. For all other cases, we

180 can therefore not include intrinsic uncertainty in our uncertainty budget. Since this uncertainty represents systematic errors

and instrumental noise, we assume no autocorrelation in the errors time-series, and propagate the errors through the ordinary

least-squares (OLS) regression:

$$\mathbf{Q}_{xx} = (\mathbf{A}' \cdot \mathbf{Q}_{yy}{}^{-1} \cdot \mathbf{A})^{-1} \tag{1}$$

Where y is our mass source change time series, $\mathbf{Q}_{yy}$ is an identity matrix with the intrinsic errors on the diagonal, and $\mathbf{A}$ is

185 the design matrix. $\mathbf{Q}_{xx}$ is used to compute the standard error of the trend (Heij et al., 2004):

$$\sigma_{trend} = \sqrt{\mathbf{Q}_{xx_{22}}} \tag{2}$$

We then use the standard error of the trend (σ_{trend}) as input in the SLE model, to see how the mass associated with the

intrinsic uncertainty is distributed over the oceans.

2.2.3 Combining Trends and Uncertainties

190 To compute total barystatic SLC and its uncertainties, we sum the individual contributions (AIS, GIS, LWS and GLA) as

follows, with a total of six combinations: CSR (all), JPL (all), IMB (AIS/GIS) + WGP (LWS/GLA), UCI (AIS/GIS) + WGP

(LWS/GLA), IMB (AIS/GIS) + GWB (LWS) + ZMP (GLA), UCI (AIS/GIS) + GWB (LWS) + ZMP (GLA).

Whereas the trends are added together linearly, we add the uncertainties in quadrature, assuming they are independent and

normally distributed. For each contribution, we first combine the different types of uncertainty following Equation (3):

195 $$\sigma_{CONTR} = \sqrt{\sigma_{temporal}^2 + \sigma_{spatial}^2 + \sigma_{intrinsic}^2} \tag{3}$$

where σ_{CONTR} is the total uncertainty for each individual contribution (AIS, GIS, GLA, LWS). We then compute the total

barystatic uncertainty for all contributions (σ_{total}) following Equation (4):

$$\sigma_{total} = \sqrt{\sigma_{AIS}^2 + \sigma_{GIS}^2 + \sigma_{LWS}^2 + \sigma_{GLA}^2} \tag{4}$$

3 Results

200 In this Section we first present the noise model selection (Section 3.1) used to compute the barystatic SL trend and temporal

uncertainty in Section 3.2. We then present the spatial-structural (Section 3.3) and intrinsic uncertainties (Section 3.4). Lastly,

we show the regional patterns of the total barystatic trends (i.e., the sum of the different contributions) and uncertainties (i.e.,

the sum of the different contributions and types of uncertainties) and zoom in on a few coastal examples (Section 3.5).

3.1 Noise characteristics of the mass sources

205 Many geophysical time-series are known to exhibit temporal (auto)correlations, as is the case for sea-level and cryosphere data (Bos et al., 2013). This autocorrelation means that each observation is not totally independent from the previous one (Bos et al., 2013), and it is defined by the shape of the spectrum of the time-series (Hughes and Williams, 2010). Understanding the shape of spectra and determining the best stochastic model to describe these spectra is important to understand the physics of the processes playing a role in the time-series (Hughes and Williams, 2010). In addition, accounting for the autocorrelation of the

210 time-series while estimating a linear trend is important both for the value of the trend itself and for the statistical error of the fit (Bos et al., 2013; Hughes and Williams, 2010). Depending on the nature of the process being studied, different noise models can be used to account for the effects of autocorrelations. Here, we determine the best noise model for each spatial data point of the mass sources of the different barystatic contributions (AIS, GIS, LWS, GLA). Our analysis shows that the optimal noise model depends on both the physical system (AIS, GIS, GLA or LWS) and the dataset (Figure 2).

215 There are clear differences between the GRACE datasets (Figure 2a-h), for which the PL and GGM noise models score higher, and the other datasets (Figure 2i-p), for which the AR(5) and AR(9) models score higher. The only exception is for the two Greenland datasets (GIS_JPL (f) and GIS_IMB (j)), where the noise model selection is reversed. Over the ice sheets, the higher resolution of GRACE observations (compared to IMBIE and UCI datasets) leads to more heterogeneity in the model selection, which suggests the inclusion/capture of more complex processes. For example, our analysis indicates that only one

220 type of noise model is selected for the entire ice sheet in the IMBIE dataset (Figure 2i-j). For LWS changes, where the spatial resolution of GRACE and the hydrological models is relatively high, the noise model selection follows a different pattern. There is a general preference for AR(1) in areas with smaller LWS changes (i.e., not the large drainage basins). On the other hand, over the large drainage basins, the same model preference mentioned above is maintained (Figure 2, right column). This suggests that GRACE observations and the hydrological models might not always be capturing the same processes.

225 Different noise models are selected as optimal for the two GRACE datasets: CSR datasets (Figure 2a-d) are best explained with the PL model, while JPL estimates (Figure 2e-h) are best explained with the GGM model. However, the GGM model is fairly similar to a pure power-law model under certain parameters. Furthermore, the noise model selection for the CSR dataset over the ice sheets (Figure 2a,b) displays an interesting pattern, which is not seen for the JPL dataset (Figure 2e,f). Regions with relatively strong ice melt (i.e., the Antarctica Peninsula, East Antarctica and northwest of Greenland) are better represented by

230 an AR(5) model. Over the extremities of the ice sheets, which are more dynamic regions, the GGM model is the optimal one. On the other hand, internal regions of the ice sheets, where there is little ablation, are better described by the PL model.

3.2 Trend and temporal uncertainty

The mass source trend and uncertainties obtained with the selected noise models (Section 3.1) are used to compute the sea-level fingerprints with the SLE model (Figure 3). To illustrate the difference between the fingerprints based on GRACE and those

235 based on GRACE-independent datasets, we show the trends and uncertainties for the JPL estimates (Figure 3a-d, i-l) and for UCI dataset for the ice sheets (Figure 3e-h) and WaterGAP for glaciers and LWS (Figure 3m-p). The classical gravitation-
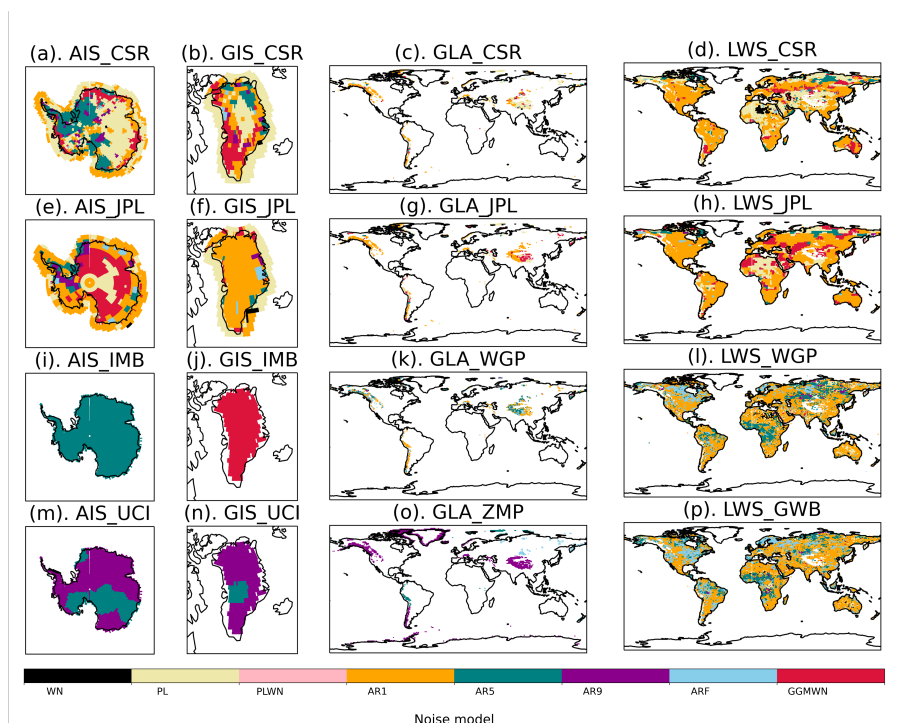
Figure 2. Noise model selection based on the time series of the different sources of mass loss for each dataset (rows) and contribution (columns), over the period 2003-2016.

rotation-deformation patterns are visible in all fingerprints: regions closer to a freshwater source present a lower SLC, due to the mass loss that causes land uplift and reduced gravitational attraction, while in the far-field the sea level rises more than average.

240   While all trends strongly depend on the dataset (Figure 3, first and third column), the uncertainty patterns are rather consistent. This suggests that, even though different noise models were used to compute the trend for each dataset, the temporal uncertainty is characteristic of each contribution. For glaciers and the ice sheets, the GRACE-independent datasets estimate a higher trend than the GRACE observations. The temporal uncertainties for ice sheets and glaciers are relatively small, especially for the UCI datasets. This indicates that these contributions do not exhibit strong autocorrelations, and as a consequence

245   the uncertainty of the trend will be small. On the other hand, the temporal uncertainty for the LWS is larger than the trend itself, and therefore the LWS trend is not statistically significant. This is probably related to the large internal and decadal variability of the time series, in combination with the relatively short period under study.

The largest inter-dataset differences are displayed in the regional patterns of the LWS contribution. Despite the similar global mean LWS trend value for both JPL and WGP, the regional trend patterns and uncertainty values are very different. This may

250   partially be related to the coarse resolution of GRACE (300 km) in comparison to the hydrological models (0.5° by 0.5° grid (55 km by 55 km at the Equator)). This difference can also be related to the difficulty in modelling the complex processes

affecting LWS, which relies on parameterisations of physical processes and on sparse observations, while GRACE measures the total mass change.

Another significant inter-dataset difference is in the regional trend pattern as a consequence of AIS mass change (Figure 255 3a,e). This is mainly related to the location of ice mass changes in each dataset. GRACE observes mass accumulation in East Antarctica, resulting in a positive sea-level trend in the region. This accumulation is not captured by the UCI data set. GRACE has a higher spatial resolution, and thus provides more detail of where the mass change is taking place. The UCI dataset provides estimates on a basin scale, so more detailed changes may be averaged out. The effect of the location of mass change at the source of the contribution is further investigated with the spatial-structural uncertainty (next section).
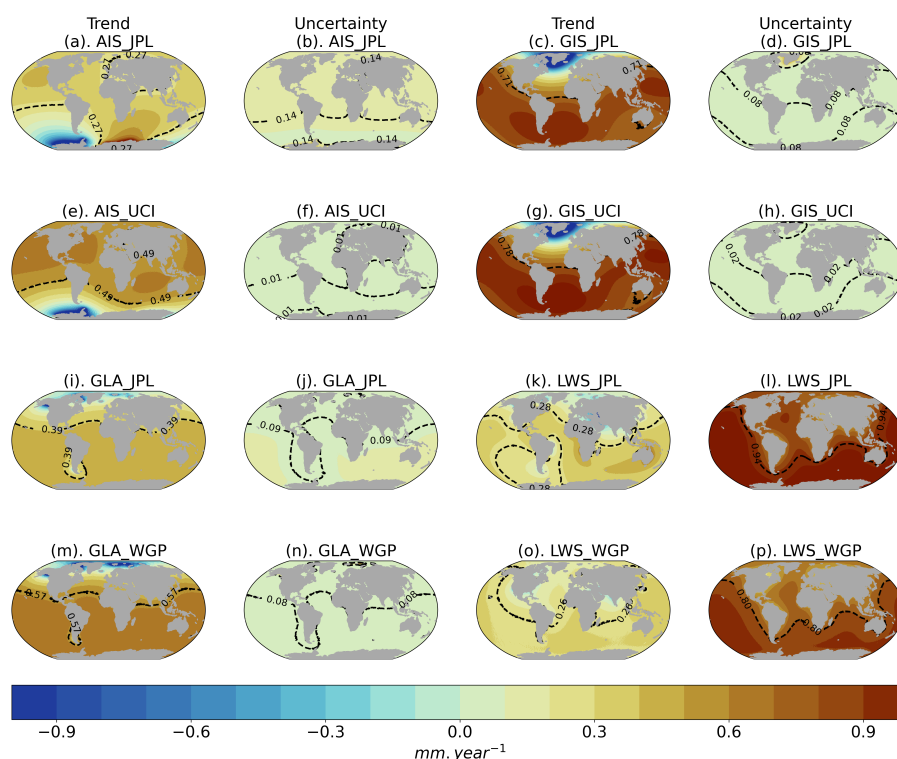
Figure 3. Regional barystatic sea-level trend and temporal uncertainty ($\mathrm{mm.year}^{-1}$) for GRACE (JPL) and independent combination (UCI + WGP) for 2003-2016. Black dashed contour line and number indicates the spatial average of the regional trend and uncertainty. Trends and uncertainties of CSR, IMB, ZMP and GWB presented in Supplementary Figure A1

260 ## 3.3 Spatial-structural uncertainty

The regional SLC fingerprints directly reflect the differences in the spatial distribution of the mass change sources of the datasets (Mitrovica et al., 2011). Over the ice sheets, for instance, IMBIE provides one time series for the entire Greenland Ice Sheet, which is subdivided into dynamic and surface mass balance changes, and the Antarctic Ice Sheet is divided into three

drainage basins. GRACE mascons, on the other hand, provide data in $0.5°$ grid cells (despite the native resolution of 300km).

265 To account for the uncertainties arising from the differences in location of the mass change between datasets, we first normalize the fingerprints and then combine them into estimates of the spatial-structural uncertainty (Figure 4).

For all contributions, the largest spatial uncertainties are concentrated closer to the mass change sources, while the uncertainties are reduced in the far field. The effect of differences resulting from Earth rotational effects (typically leading to four large quadrants) is visible in the far field of the AIS (in the Northern Pacific) and of hotspots of LWS (around the Southern Ocean).

270 As was the case for the trends (Figure 3a), the AIS shows the strongest spatial differences, as the underlying datasets strongly differ in their spatial detail. The spatial uncertainties represent the error introduced by using datasets that have insufficient resolution to solve the processes being analysed. In addition, it also shows that different physical processes are captured by the different datasets, as is the case for the LWS estimate. The LWS models have higher resolution than the GRACE observations, nonetheless the spatial-structural uncertainty of LWS component (Figure 3d) is the second largest.
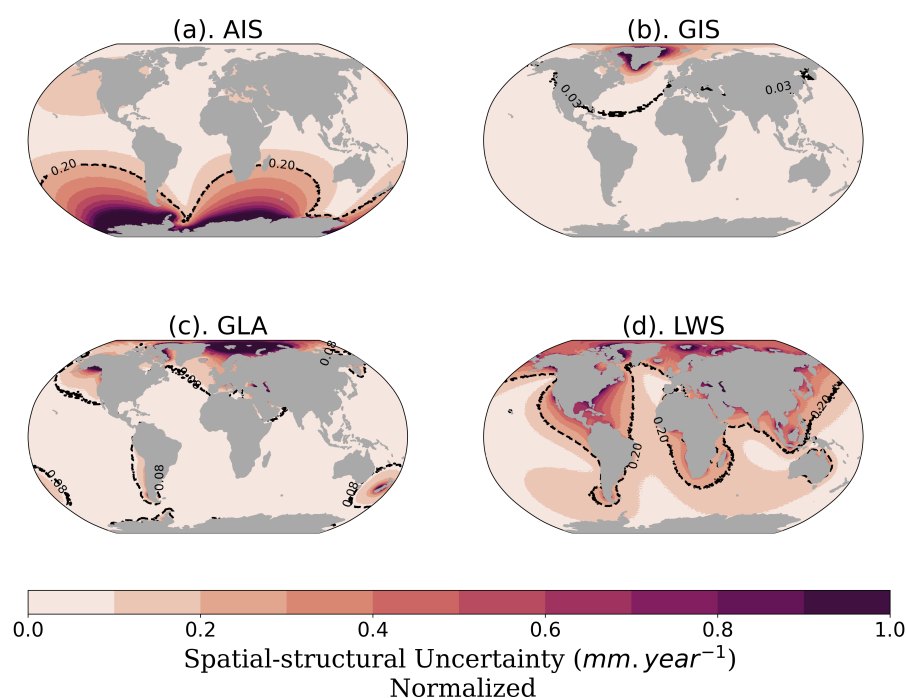
Figure 4. Normalised regional barystatic sea-level change fields of the spatial-structural uncertainty (0-1 mm.year^{-1}), representing the uncertainty arising from the different locations of mass changes for Antarctica (a), Greenland (b), glaciers (c) and land water storage (d). Black dashed contour line and number indicates the spatial average of the regional uncertainty.

3.4 Intrinsic uncertainty

The final type of uncertainty considered here is the intrinsic uncertainty, which represents noise related to the dataset itself. This type of uncertainty arises from the processing of the data, and needs to be provided with the model/observation. This information is only available for the JPL and IMBIE datasets (Figure 5). All intrinsic uncertainties are fairly small (note that the colorbar ranges only up to 0.10 mm.year^{-1}). The maximum uncertainty is seen in the LWS contribution (Figure 5a), with maximum values reaching 0.07 mm.year^{-1}. Additional analysis (not shown) where the intrinsic uncertainty was computed based on (i) the linear trend of the errors time series and (ii) propagated using the upper-lower bound method confirm the small values of the intrinsic uncertainty. The IMBIE datasets (Figure 5e,f) show a slightly larger intrinsic uncertainty ice sheets uncertainties from JPL (Figure 5c,d), which is expected as the IMBIE is an ensemble of several datasets and methods. Overall, the intrinsic uncertainty, which is dependent of the observational technique, is relatively small when compared to the spatial-structural and temporal uncertainties, which are related to the physical processes represented.
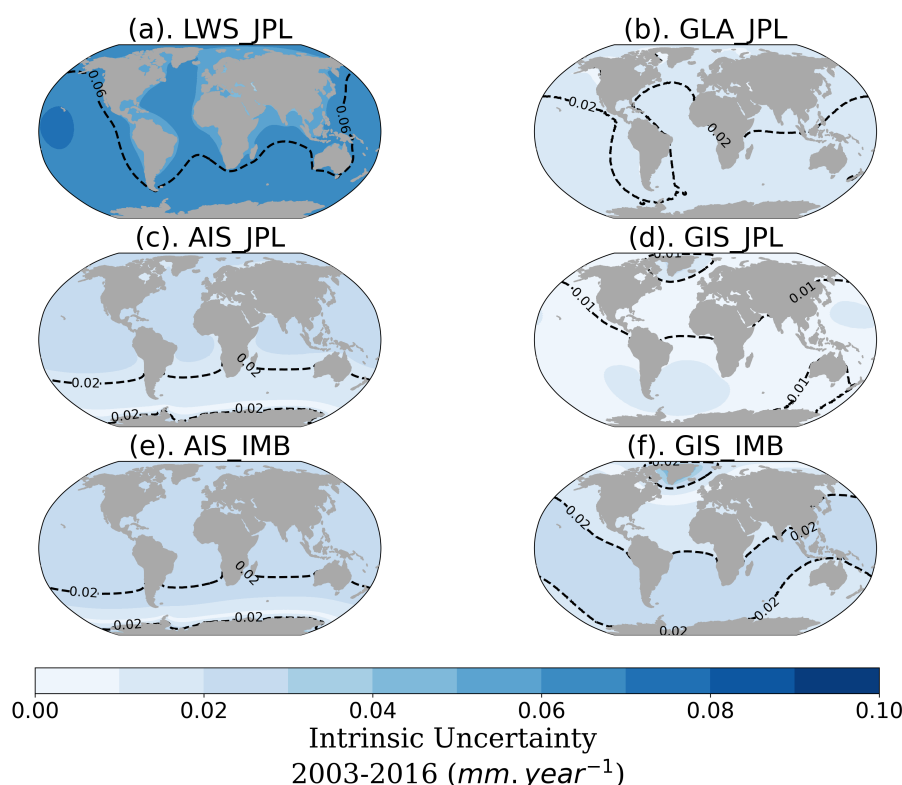
Figure 5. Regional barystatic sea level fields of the intrinsic uncertainty (mm.year^{-1}) for the land water storage (a), glaciers (b), Antarctica (c) and Greenland (d) contributions of the JPL dataset; and Antarctica (e) and Greenland (f) contributions of the IMBIE dataset. Black dashed contour line indicates the spatial average of the regional uncertainty

3.5 Total Barystatic Trend and Uncertainty

Combining the different contributions, as explained in Section 2.2.3, leads to the total barystatic trends and uncertainties shown in Figure 6. Although we analysed six barystatic combinations, here we show only two (JPL and IMB+WGP) to discuss the patterns and the total uncertainty fields. We show these specific combinations because they present the most complete uncertainty budget (as only JPL and IMB had intrinsic uncertainties). Additional combinations are presented in Supplementary Figure A2, with the global mean values listed in Supplementary Table A1. We recall that the aim of this study is not to provide one final ensemble of the barystatic contribution, but rather to focus on the uncertainty budget. Figure 6 shows the JPL GRACE dataset (panels a-b) and the combination of IMBIE and WaterGAP (c-f), the latter for both the common period of 2003-2016 (a-d) and the longer period of 1993-2016 (e-f). When all the contributions are combined, we find that the regional barystatic sea-level trends range from -0.43 to 2.55 mm.year^{-1} for 2003-2016, and from -0.39 to 2.00 mm.year^{-1} for 1993-2016, depending on the dataset choice and the location. When all types of uncertainties from all contributions are combined, the total barystatic uncertainties range from 0.62 to 1.29 mm.year^{-1} for 2003-2016, and from 0.35 to 0.90 mm.year^{-1} for 1993-2016, also depending on the dataset choice and location.

For most regions of the world, we find that the regional barystatic sea-level trend is higher than the 1-sigma total uncertainty, with exception of the regions near the polar areas (indicated by stipples in Figure 6). Comparing the JPL trend to the IMB+WGP trend, the shape of the pattern is similar, but the global mean (and thereby the regional SLC) is larger for JPL. This is also reflected by the histograms of the regional trend (depicted below the maps), which indicate larger regional SLC values for the JPL dataset (locally ranging from -0.43 to 2.19 mm.year^{-1}) than for the IMB+WGP combination (locally ranging from -0.10 to 1.69 mm.year^{-1}). The regional histograms also show a clearly skewed distribution of the trend, with mainly positive values. When we compare the two periods of IMB+WGP (Figure 6c, e), the regional histogram is slightly narrower for the longer period (i.e., less divergence for the regional values), ranging from -0.39 to 1.50 mm.year^{-1}. This is probably because the local effect of internal variability plays a smaller role in the longer period. Nonetheless, the regional pattern is similar for both periods.

The uncertainty patterns (Figure 6, right panels) are similar for the different dataset combinations (JPL vs. IMB+WGP) and periods (2003-2016 vs. 1993-2016). JPl regional uncertainties range from 0.62 to 0.98 mm.year^{-1}, while the IMB+WGP combination ranges from 0.62 to 1.02 mm.year^{-1}, both for the 2003-2016 period. Just like for the trend, the longer period IMB+WGP uncertainties have a similar pattern but with lower values than for the shorter period, with regional values ranging from 0.37 to 0.75 mm.year^{-1}. Although the total uncertainty is dominated by the temporal uncertainty (see Figure 7), the similarity of the uncertainty pattern for both periods is influenced by the fact that the spatial-structural errors are based on the 2003-2016 period and extended to 1993-2016. On average, the spatial-structural uncertainty represents 16% (25%) of the total uncertainty, while the temporal represents 80% (70%), for the 2003-2016 (1993-2016) period.

To further illustrate how the different contributions and uncertainties contribute to the total uncertainty budget, we selected ten coastal cities around the world in which we break down the total uncertainty of barystatic SLC from 1993-2016 into the four
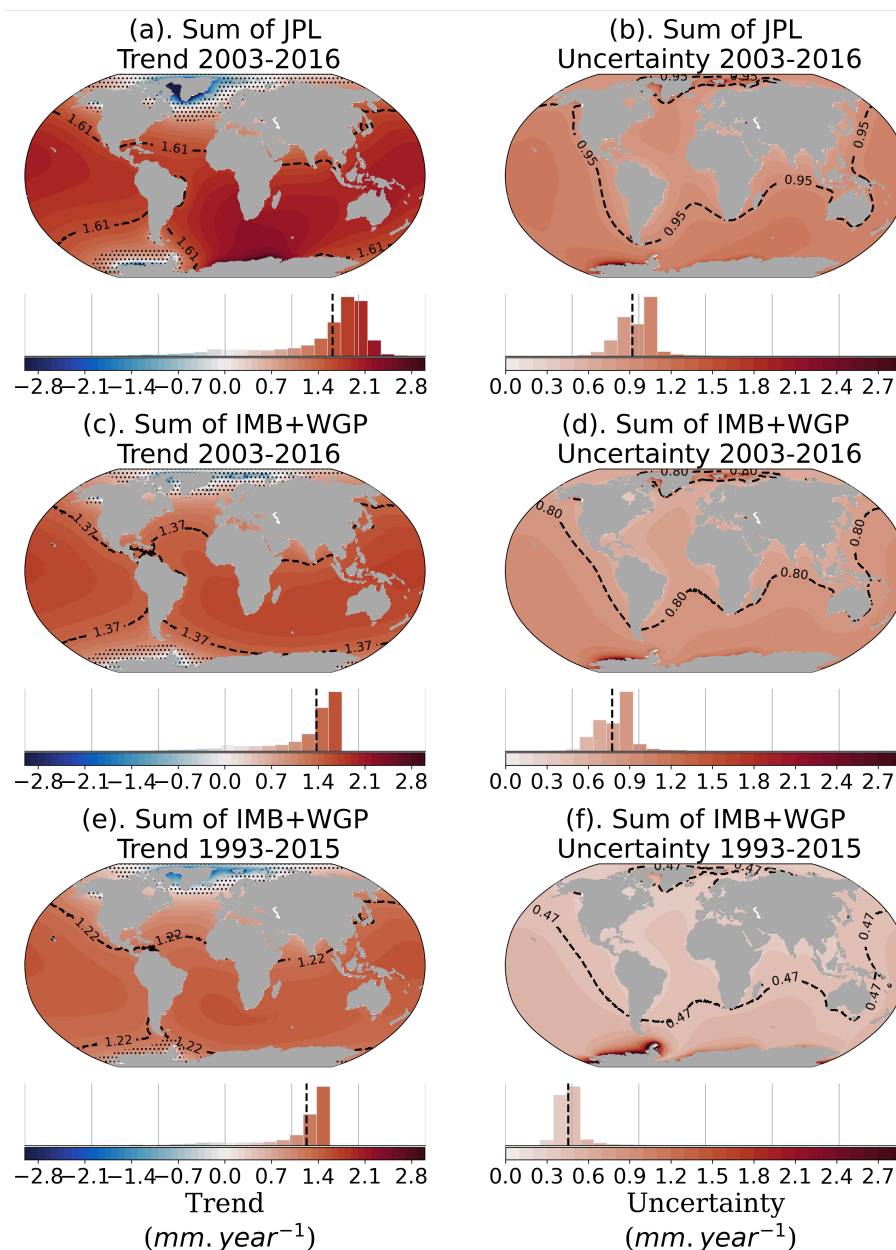
Figure 6. Total regional barystatic SLC fields of the trend and uncertainty $(\mathrm{mm.year}^{-1})$ (AIS+GIS+LWS+Glaciers contributions; intrinsic + temporal + spatial uncertainties) for GRACE (a,b) and IMBIE+WaterGAP for 2003-2016 (c,d) and for 1993-2016 (e,f). Histograms underneath each map indicates the distribution of the regional values across the oceans. Spatial average of the regional trend and uncertainty indicated by black dashed lines in the maps and bar charts. Regions with trends smaller than the 1-sigma uncertainty are indicated in the map with stipples.

contributions (Figure 7a), and into the three types of uncertainties (Figure 7b). We also show the different types of uncertainties
320 for each of the contributions (Figure 7c). As in in Figure 6, we show the IMB+WGP combination.

The large contribution of the LWS and temporal uncertainty to the uncertainty budget is highlighted on Figure 7. Figure 7a shows that the LWS uncertainty plays an important role at all locations, being responsible for at least 50% of the total uncertainty. While the temporal uncertainty is the main contribution of the LWS uncertainty (Figure 7c), in some locations, such as Washington (US, location 3) and Tokyo (Japan, location 9) the spatial uncertainty is also important. Even without the
325 contribution of LWS to the total uncertainty (Supplementary Figure A5), the temporal uncertainty is still the main contributor.

The second main contribution to the uncertainty budget comes from the AIS and glaciers (GLA). In these examples, the relative importance of AIS and GLA is fairly similar, with exception of Vancouver (Canada, location 1), for which the glaciers contribute about 5 times more than AIS. For the GLA, the dominant type of uncertainty strongly depends on the location (Figure 7c). For example, in Vancouver (Canada, location 1), Lima (Peru, location 2) and Rotterdam (The Netherlands, location
330 5), the spatial-structural uncertainty dominates the contribution from GLA. In all other locations, the intrinsic and temporal uncertainties play a more important role in the GLA contribution to the uncertainty budget. The AIS uncertainty is mainly dominated by the temporal uncertainty, with exception of Cape Town (South Africa, location 6), which is located within the large uncertainty bulge of the spatial-structural uncertainty from AIS (see Figure 4a).

The GIS and intrinsinc uncertainty play a small role in the uncertainty budget. On average, the GIS is only responsible for
335 about 10% of the total uncertainty (panel a), and its uncertainty is generally dominated by the intrinsic and spatial uncertainties rather than temporal uncertainties (panel c). The intrinsic uncertainty (panel b) is fairly small in all locations. Even for the JPL combination (Supplementary Figure A4), which has intrinsic uncertainty estimation for all contributions, the intrinsic uncertainty is responsible, on average, for only 5% of the total uncertainty.

4 Discussion and Conclusion

340 In this manuscript we investigate the barystatic contribution to regional sea-level trends over 1993-2016 and 2003-2016, focusing on improving the understanding of the uncertainty budget. We show how mass changes of glaciers, land water storage, and the Greenland and Antarctic ice sheets influence regional SLC by computing sea-level fingerprints. We consider three types of uncertainties in our budget: the determination of a linear trend (temporal); the spread around a central estimate as influenced by the distribution of mass change sources (spatial); and the uncertainty from the data/model itself (intrinsic). We find that
345 the intrinsic uncertainty has a fairly small contribution to the total uncertainty. The uncertainty budget is dominated by the temporal uncertainty, followed by a significant contribution of the spatial-structural uncertainty.

We find that the total regional barystatic sea-level trends range from -0.10 to 1.69 mm.year^{-1} for 2003-2016, and from -0.39 to 1.50 mm.year^{-1} for 1993-2016, depending on location, for the IMB+WGP combination. Our total uncertainty in the regional barystatic sea-level trend ranges from 0.62 to 1.02 mm.year^{-1} for 2003-2016, and from 0.37 to 0.75 mm.year^{-1}
350 for 1993-2016 for the IMB+WGP combination, with spatial averages of 0.80 and 0.47 mm.year^{-1}, respectively. While these values may seem large compared to studies focusing on global changes alone (Horwath et al., 2021; Frederikse et al., 2020),
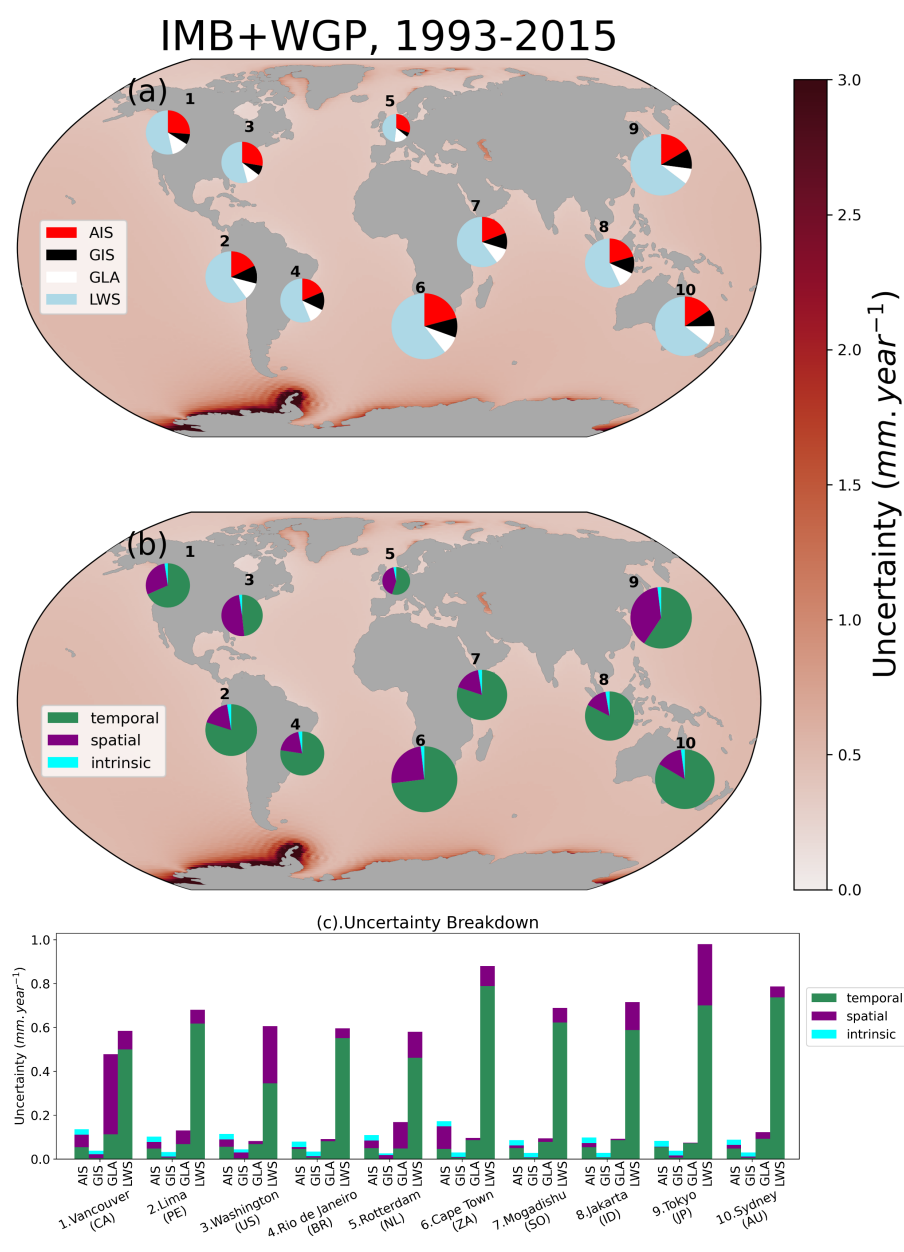
Figure 7. Pie charts represent the total uncertainty separated by (a) contribution and (b) type of uncertainty, and the bars the breakdown for each contribution (c). Background maps show the total barystatic uncertainty. The size of the pie charts is relative to the magnitude of the total uncertainty. Note that the uncertainties are combined in quadrature, so simply adding up the bars in panel c will not reflect the size of the pie charts on panels a and b.

other studies also found that regional uncertainties are higher than the previously published global mean rates (Prandi et al., 2021; Bos et al., 2014). For example, in a recent satellite altimetry sea-level change assessment, Prandi et al. (2021) found that the local sea-level trend uncertainty due to observational errors (i.e., intrinsic uncertainties) was about two times higher than

355   the global mean sea-level trend uncertainty of Ablain et al. (2019). We note that the spatial average of the regional uncertainties (indicated by the black dashed line in the figures) is not equal to the uncertainty of the global mean barystatic SLC time series and trend, once our uncertainty assessment is focused on the regional sea-level change fields. As a consequence the spatial averages will lead to larger values then the uncertainty of the global mean sea-level time series (see Figure A3). Thus, one should not compare the value given here to characterize global mean sea-level changes with other studies focusing on the

360   global mean. (e.g. Horwath et al. (2021))

Our regional barystatic sea-level trends clearly show the classical gravitational-rotational-deformational pattern, matching qualitatively with other fingerprints (e.g., Mitrovica et al. (2001); Riva et al. (2010); Hsu and Velicogna (2017); Jeon et al. (2021)). Our spatial-structural uncertainties highlight the effect of using a uniform mass change (i.e., only one value averaged over a region) compared to non-uniform local mass changes (Bamber and Riva, 2010; Mitrovica et al., 2011). For example, we

365   show that different location of mass changes can lead to deviations larger than 20% for AIS (Figure 4). As a consequence of the relatively low spatial resolution of the observations, the AIS is the second main contributor to the total barystatic uncertainty budget. Furthermore, we show that this effect is important not only for AIS, but for all the barystatic contributions.

The main source of uncertainty in the barystatic SLC is the temporal uncertainty from the land water storage (LWS) contribution. This is likely related to the natural variability of LWS (Vishwakarma et al., 2021; Hamlington et al., 2017; Nerem et al.,

370   2018), which is mainly driven by seasonal and interannual cycles (Cáceres et al., 2020). A method to deal with the LWS natural variability would be to use different metrics than linear trends(Vishwakarma et al., 2021), as the use time varying trends based on a state space model (Frederikse et al., 2016; Vishwakarma et al., 2021). However, we choose to use in this study linear trends for sake of accuracy, reproducibility and discussion. It has also been suggested that a more appropriate way of computing a meaningful linear trend from LWS is to incorporate this variability in the analysis (Vishwakarma et al., 2021), as we did by

375   including the seasonal components in the functional model. Nonetheless, the LWS uncertainties related to the trend were still very high, suggesting that that a period of 25 years (1993-2016) might still be too short to solve the low frequency natural variability of LWS, particularly on (multi)-decadal timescales.

In this work we provide an assessment of the uncertainties related to the barystatic contribution to regional SLC, in particular about the spatial distribution of the uncertainties. Our results highlight that improving the spatial detail of land ice mass loss

380   products, as well as determining more accurate land water storage trends, would lead to better SLC estimates. In addition, our findings can be used to inform projection frameworks. For example, we show that the distribution of ice in the Antarctica Ice Sheet has a significant impact on regional SLC, even in locations far from the ice sheets, such as The Netherlands. This means that, depending on the region of a collapse in the Antarctica Ice Sheet, the sea-level rise projections, which are often based on uniform ice sheet distributions and static fingerprints (e.g., Slangen et al. (2012); Jevrejeva et al. (2019)) , may have

385   large regional deviations due to spatial differences in the mass source. Incorporating the insights of uncertainty assessments in sea-level frameworks (as in Larour et al. (2020)) should eventually lead to better sea-level projections.

390 **Appendix A: Data Description**

The datasets used in this manuscript are briefly described below. In-depth description of each dataset can be found in their respective references.

A1 GRACE Mascon Estimates

We use GRACE land mass concentrations (mascons) solutions from two processing centers: RL06 v02 from CSR (Save et al.,
395 2016; Save, 2020) and RL06 v02 from Jet Propulsion Laboratory (JPL) (Watkins et al., 2015; Wiese et al., 2019). We chose to use the mascons solution instead of spherical harmonics to avoid the land-ocean leakage issue (Jeon et al., 2021; Chambers et al., 2007). The mascons include all mass changes in the Earth system, accounting for variations in land hydrology and in the cryosphere, as well as solid Earth motions (Adhikari et al., 2019). We do not, however, use the changes in the ocean, since we focus on land hydrology and cryosphere variations. CSR and JPL mascons are provided on a 0.25 and 0.5 degree
400 grids, respectively, even though the native resolution of the GRACE/GRACE-FO data is roughly 300km (i.e., 3-degree equal-area mascons). Both mascons have been corrected for glacial isostatic adjustment (GIA) with the ICE6G-D model (Peltier et al., 2018), and for ocean and atmosphere dealiasing (AOD1B 'GAD' fields). In addition, the JPL mascons use a Coastline Resolution Improvement (CRI) filter to separate land/ocean mass within the mascon (Wiese et al., 2016). Only the JPL mascons are provided with intrinsic uncertainty estimates (Wahr et al., 2006; Wiese et al., 2016). Both mascons are given with a monthly
405 frequency, ranging from April-2002 to August-2020.

A2 IMBIE Estimates

For both ice sheets we use the products of IMBIE (Shepherd et al., 2018, 2020), which combines several estimates (26 for GIS and 24 for AIS) of ice sheet mass balance derived from satellite altimetry, satellite gravimetry and the input-output method. The monthly datasets cover the period 1992-2017 and 1993-2018 for AIS and GIS, respectively. In addition to the total ice
410 sheet mass balance, the GIS dataset also distinguishes between surface mass balance (GRE SMB) and dynamic ice discharge (GRE DYN). For the AIS, the data is subdivided in the main 3 drainage regions: West Antarctica, East Antarctica and the Antarctic Peninsula. The IMBIE estimates are provided with intrinsic uncertainty estimates, reflecting the combination of several different datasets.

A3 UCI AIS and GIS Estimates

415 Using improved records of ice thickness, surface elevation, ice velocity and a surface mass balance model (RACMOv2.3), Mouginot et al. (2019) and Rignot et al. (2019) present yearly reconstructions of mass changes from the 1970s until 2017

and 2018 for the Greenland and Antarctica ice sheets, respectively. These GRACE-independent reconstructions agree, within uncertainties, with estimates from radar and laser altimetry and GRACE. The reconstructions are provided as the mean for each drainage basin, based on ice velocity data (18 basins for AIS (Rignot et al., 2011) and 6 for GIS (Mouginot and Rignot,
420   2019)).

A4   WaterGAP Hydrological Model

We use the integrated version of the WaterGAP global hydrological model (Döll et al., 2003) v2.2d with a global glacier model (Marzeion et al., 2012), presented in Cáceres et al. (2020). The hydrological model uses a homogeneized climate forcing from WFDEI (Weedon et al., 2014), with the precipitation correction of GPCC (Schneider et al., 2015). The model is provided on a
425   0.5 degree grid, covering all continental areas except for Antarctica. In order to consistently treat both ice sheets (GIS and AIS), we remove Greenland from the model. The WaterGAP model simulates human water use, daily water flows and water storage, taking into account dams and reservoirs based on the GRanD database (Lehner et al., 2011) and assuming that consumptive irrigation water use is 70% of the optimal level in groundwater depletion areas. The glacier model computes mass changes for individuals glaciers around the world (based on the Randolph Glacier Inventory (Pfeffer et al., 2014), including glaciers
430   surface mass balance, glacier geometry, air temperature and several others glacier-specific parameters and variables (Marzeion et al., 2012). The dataset is provided at a monthly frequency, from 1948-2016.

A5   PCR-GLOBWB Hydrological Model

The second global hydrological model included in our analysis is the PCRaster Global Water Balance 2 model (PCR- GLOBW, Sutanudjaja et al. (2018)), which fully integrates different water uses, such as water demand, groundwater and surface water
435   withdrawal, water consumption, with the simulated hydrology. The model is forced with the W5E5 version 1 (Lange, 2019), covering the period 1979-2016. It provides monthly averages of total water storage thickness with a 5 arcmin resolution. Dams and reservoirs form the GRanD database (Lehner et al., 2011) are also included in the model. As this model does not explicitly resolve glaciers nor includes ice sheets, we mask out all the glaciated areas.

A6   Zemp 2019 Glacier data

440   We use the yearly glacier mass loss estimates from Zemp et al. (2019) over the period 1961 to 2016. This dataset combines the temporal variability from the glaciological data, computed using a spatio-temporal variance decomposition, with the glacier-specific values of the geodetic observations. Both glaciolocial and geodetic observations comes from the World Glacier Monitoring Service (WGMS, 2021). This combined data is then statistically extrapolated to the full glacier sample to assess regional mass changes, taking into account regional rates of area change. This dataset provides regional mass changes for the
445   19 regions of the Randolph Glacier Inventory (Consortium, 2017; Pfeffer et al., 2014).

Appendix B: Supplementary Figures and Tables
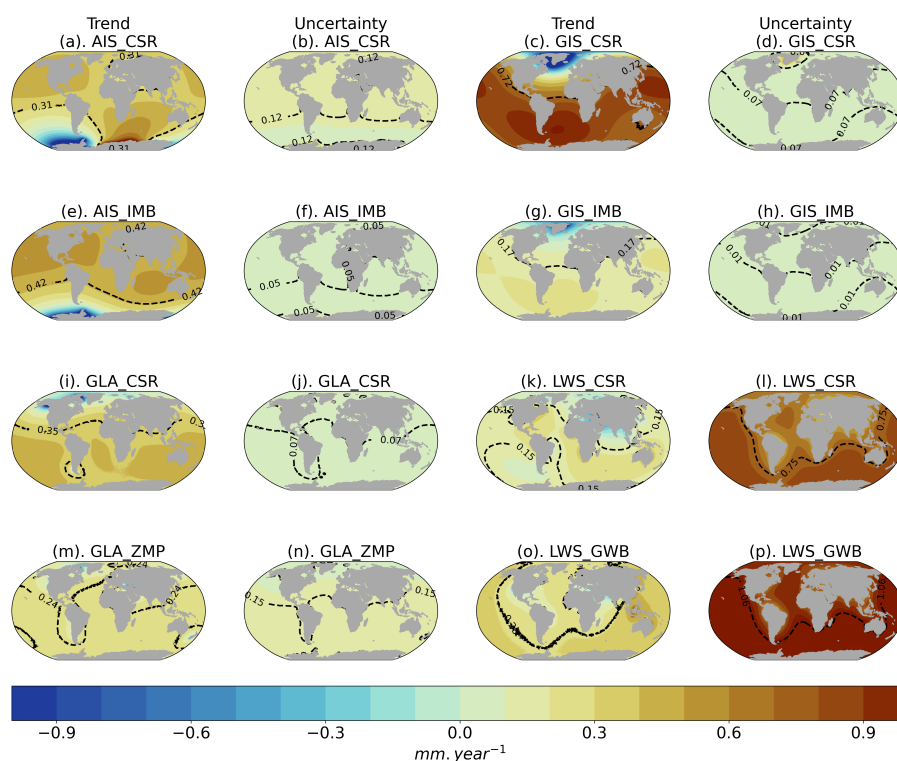
Figure A1. Regional barystatic sea-level trend and temporal uncertainty ($\mathrm{mm.year^{-1}}$) for GRACE (CSR) and independent combination (IMB + ZMP + GWB) for 2003-2016. Black dashed contour line and number indicates the spatial average of the regional trend and uncertainty. Complementary of trends and uncertainties of Figure 3.
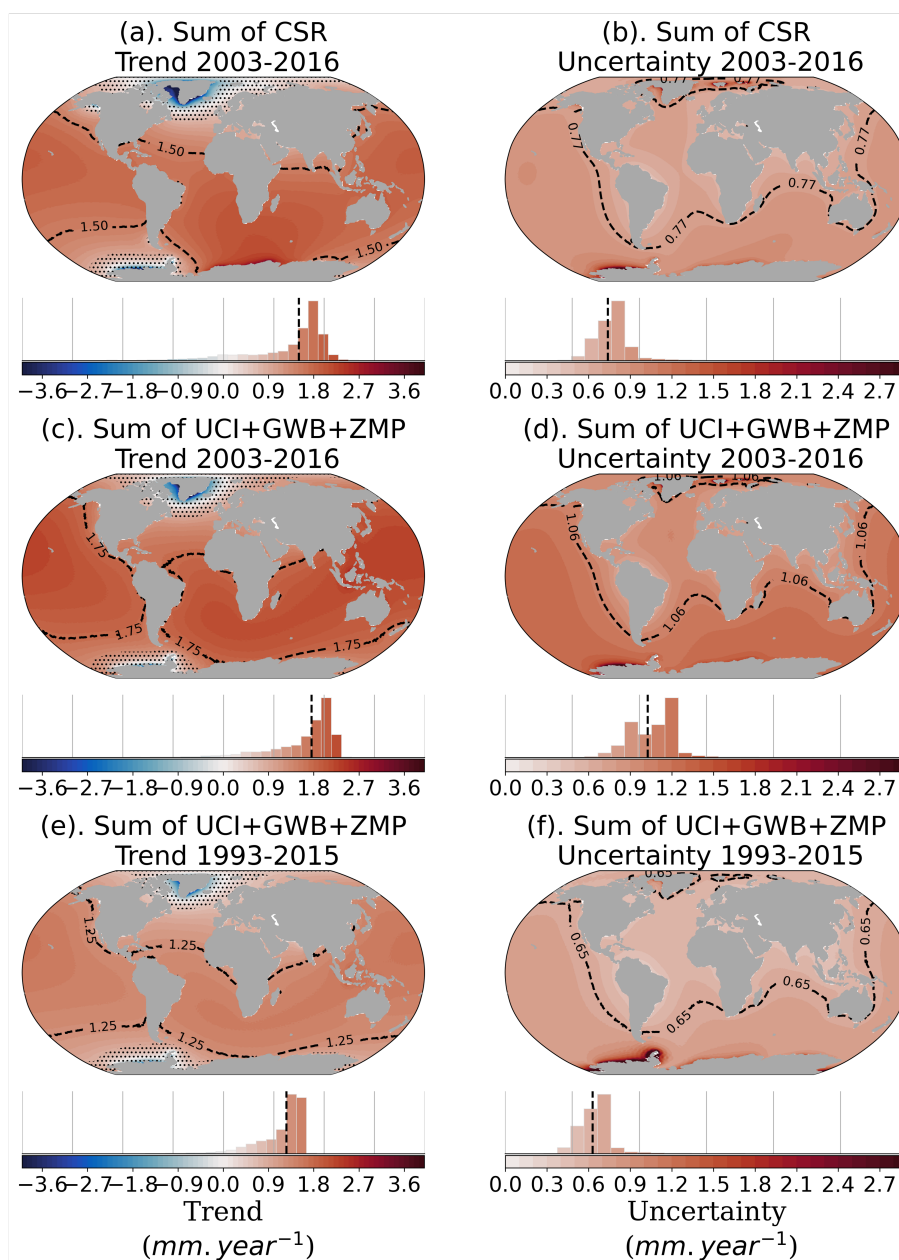
Figure A2. Total regional barystatic SLC fields of the trend and uncertainty (mm.year^{-1}) (AIS+GIS+LWS+Glaciers contributions; intrinsic + temporal + spatial uncertainties) for GRACE CRS (a,b) and UCI + GlobWEB + Zemp for 2005-2015 (c,d) and for 1993-2016 (e,f). Histograms underneath each map indicates the distribution of the regional values across the oceans. Spatial average of the regional trend and uncertainty indicated by black dashed lines in the maps and bar charts. Complementary of trends and uncertainties of Figure 6.
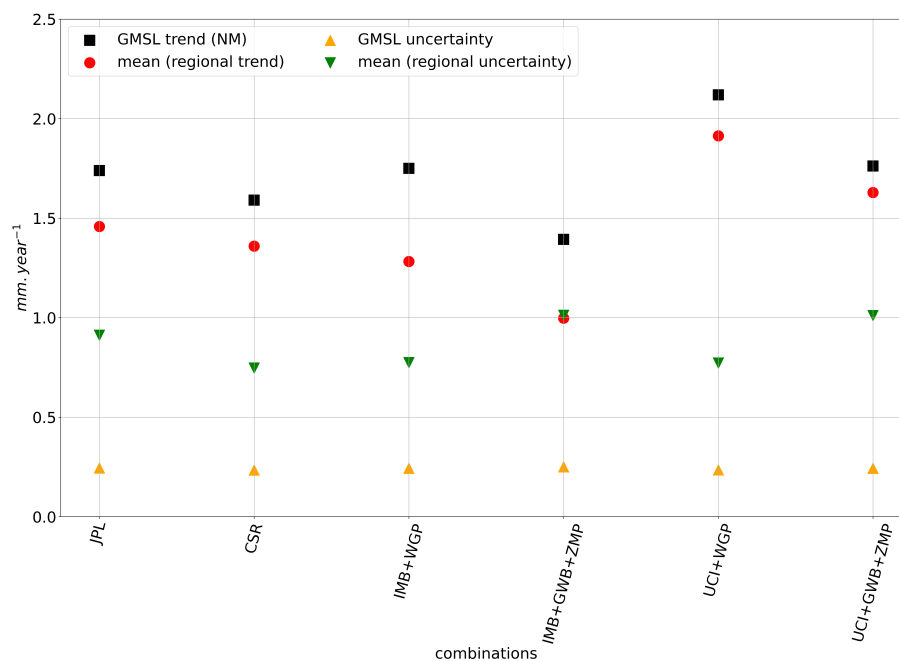
Figure A3. Comparison of global mean sea-level trend (black squares) and uncertainty (yellow traingles) with the spatial average of the regional trend (red circles) and uncertainty (green upside down triangles) from 2003-2016. The difference between the GMSL trend and spatial average of the regional trend is due to the use of regionally different noise models (following selection of Figure 2)
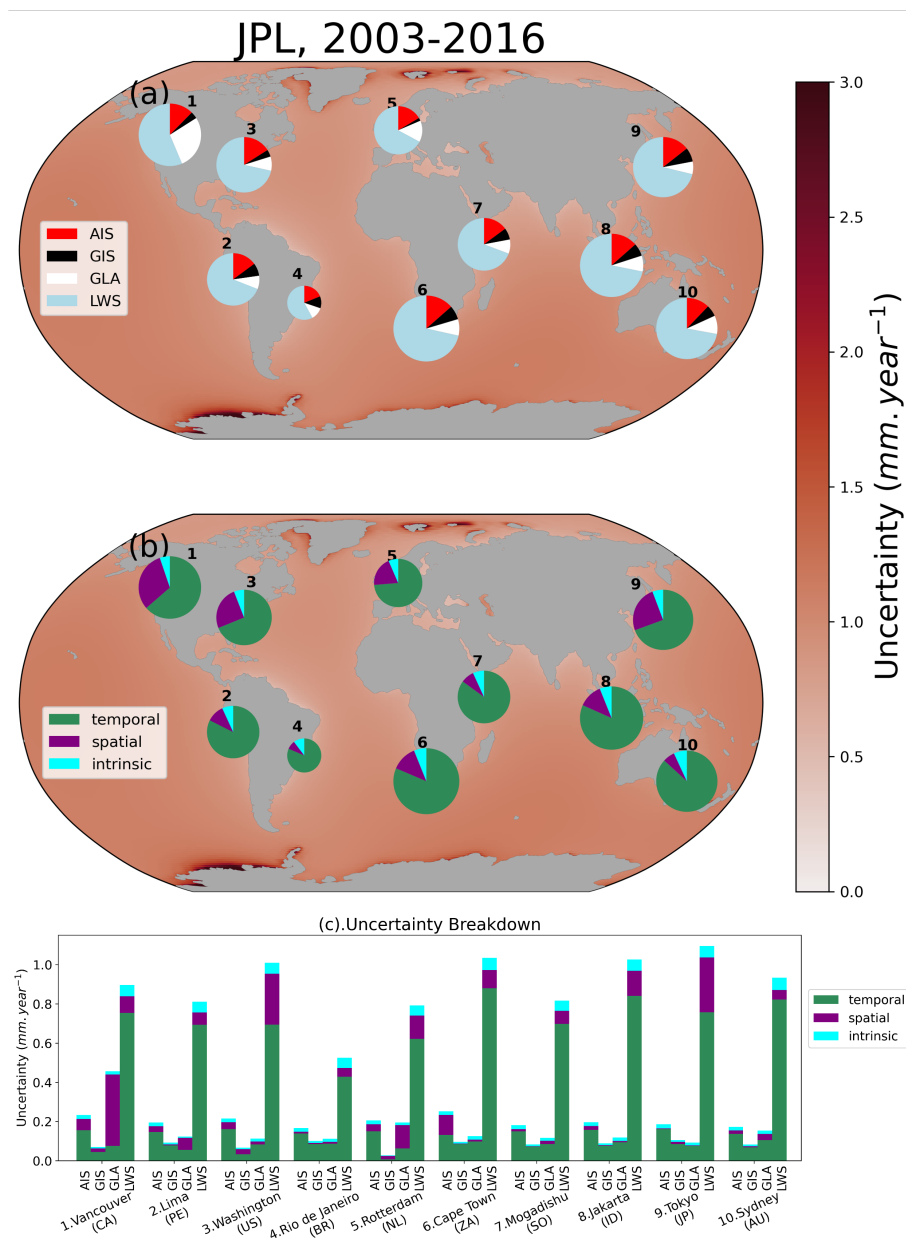
Figure A4. Same as Figure 7, for JPL dataset, from 2003-2016.
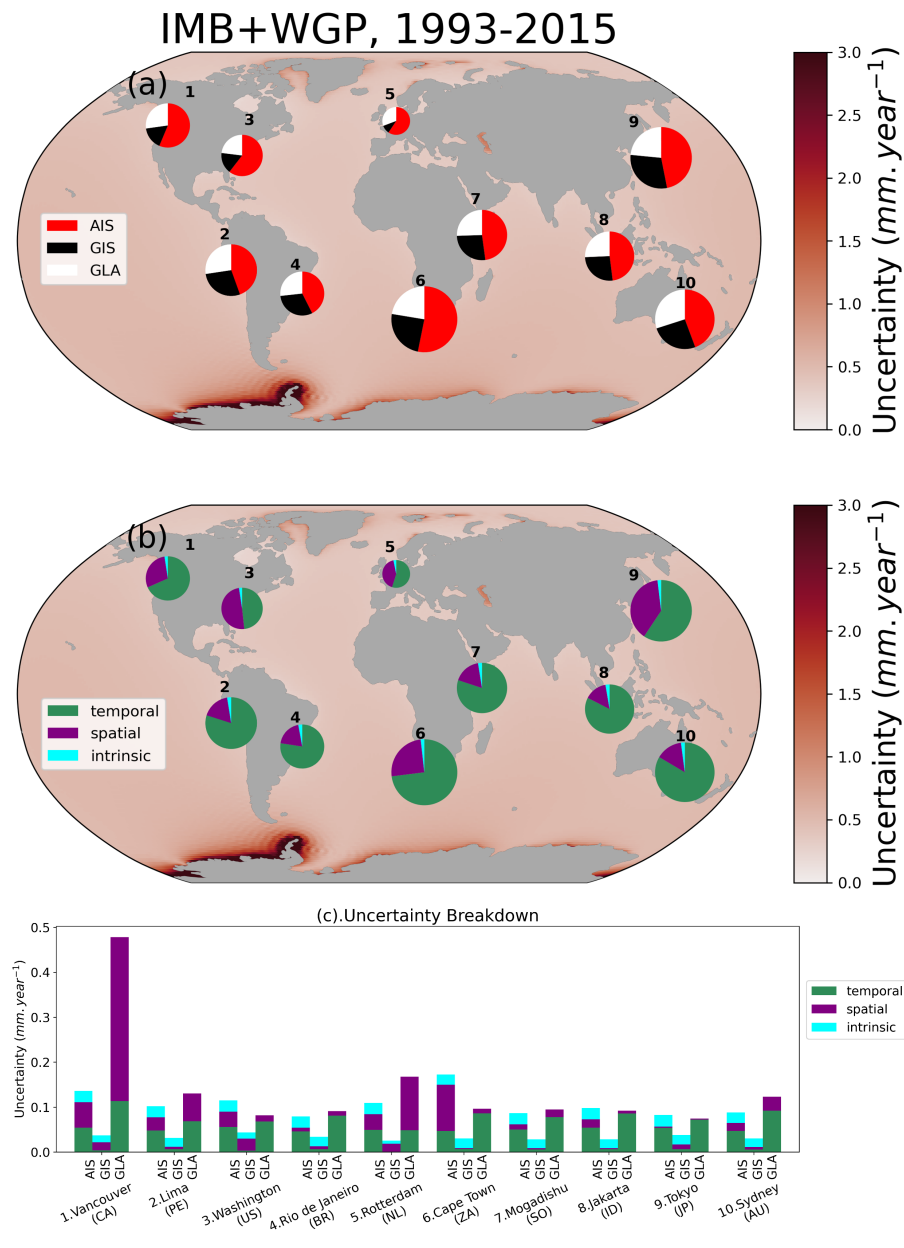
Figure A5. Same as Figure 7, but without the contribution of land water storage (LWS)

Table A1. Table with global mean barystatic sea-level changes and uncertainties from the original global mean timeseries. Note that these numbers may be different compared to the histograms of Figure 6, which represent the spatial average of the regional trend and uncertainty. The difference between the trends is due to the use of noise-models for the regional trend, against an ordinary least-squares fit for the global mean trend.

	2003-2016			1993-2016		
	trend	±	unc	trend	±	unc
AIS						
AIS_CSR	0.31	±	0.11			
AIS_JPL	0.27	±	0.11			
AIS_IMB	0.34	±	0.12	0.25	±	0.12
AIS_UCI	0.51	±	0.10	0.39	±	0.10
GIS						
GIS_CSR	0.74	±	0.09			
GIS_JPL	0.75	±	0.09			
GIS_IMB	0.62	±	0.09	0.41	±	0.08
GIS_UCI	0.82	±	0.08	0.51	±	0.08
GLA						
GLA_CSR	0.36	±	0.15			
GLA_JPL	0.39	±	0.15			
GLA_WGP	0.57	±	0.15	0.49	±	0.16
GLA_ZMP	0.20	±	0.15	0.27	±	0.15
LWS						
LWS_CSR	0.18	±	0.11			
LWS_JPL	0.32	±	0.12			
LWS_WGP	0.22	±	0.12	0.24	±	0.08
LWS_GWB	0.24	±	0.13	0.33	±	0.08
Combination						
CSR	1.59	±	0.23			
JPL	1.74	±	0.24			
IMB+WGP	1.75	±	0.24	1.38	±	0.23
IMB+GWB+ZMP	1.39	±	0.25	1.26	±	0.23
UCI+WGP	2.12	±	0.24	1.62	±	0.22
UCI+GWB+ZMP	1.76	±	0.24	1.49	±	0.22

Author contributions. CC performed the research and drafted the article. CC, RR and AS designed the study. All authors contributed to the interpretation of the results and the writing of the manuscript.

Competing interests. The authors declare that they have no conflict of interest.

450 *Acknowledgements.* This research was funded by the Netherlands Space Office User Support program (grant no. ALWO.2017.002). All figures were done in python, using scientific colour maps from Crameri (2018) and from Thy (2016).

References

True colors of oceanography., Oceanography, 3, https://doi.org/http://dx.doi.org/10.5670/oceanog.2016.66, 2016.

Ablain, M., Meyssignac, B., Zawadzki, L., Jugier, R., Ribes, A., Cazenave, A., and Picot, N.: Uncertainty in Satellite estimate of Global Mean
  Sea Level changes, trend and acceleration, Earth System Science Data Discussions, 58344, 1–26, https://doi.org/10.5194/essd-2019-10,
  2019.

Abram, N., Gattuso, J.-P., Prakash, A., Cheng, L., Chidichimo, M., Crate, S., Enomoto, H., Garschagen, M., Gruber, N., Harper, S., Holland,
  E., Kudela, R., Rice, J., Steffen, K., and von Schuckmann, K.: Framing and Context of the Report, in: IPCC Special Report on the Ocean
  and Cryosphere in a Changing Climate, In press., 2019.

Adhikari, S., Ivins, E. R., Frederikse, T., Landerer, F. W., and Caron, L.: Sea-level fingerprints emergent from GRACE mission data, Earth
  System Science Data Discussions, pp. 1–22, https://doi.org/10.5194/essd-2019-3, 2019.

Akaike, H.: A new look at the statistical model identification, IEEE Trans. Automat. Contr., p. 716–723,
  https://doi.org/10.1109/TAC.1974.1100705, 1974.

Amante, C. and Eakins, B. W.: ETOPO1 1 Arc-Minute Global Relief Model: Procedures, Data Sources and Analysis, NOAA Technical
  Memorandum NESDIS NGDC-24. National Geophysical Data Center, NOAA, https://doi.org/https://doi.org/10.7289/V5C8276M, 2009.

Bamber, J. and Riva, R.: The sea level fingerprint of recent ice mass fluxes, The Cryosphere, 4, 621–627, https://doi.org/10.5194/tc-4-621-
  2010, 2010.

Bos, M. S., Fernandes, R. M., Williams, S. D., and Bastos, L.: Fast error analysis of continuous GNSS observations with missing data,
  Journal of Geodesy, 87, 351–360, https://doi.org/10.1007/s00190-012-0605-0, 2013.

Bos, M. S., Williams, S. D., Araújo, I. B., and Bastos, L.: The effect of temporal correlated noise on the sea level rate and acceleration
  uncertainty, Geophysical Journal International, 196, 1423–1430, https://doi.org/10.1093/gji/ggt481, 2014.

Cáceres, D., Marzeion, B., Malles, J. H., Gutknecht, B., Müller Schmied, H., and Döll, P.: Assessing global water mass transfers from con-
  tinents to oceans over the period 1948-2016, Hydrology and Earth System Sciences Discussions, pp. 1–37, https://doi.org/10.5194/hess-
  2019-664, 2020.

Camargo, C. M. L., Riva, R. E. M., Hermans, T. H. J., and Slangen, A. B. A.: Exploring Sources of Uncertainty in Steric Sea-Level Change
  Estimates, Journal of Geophysical Research: Oceans, pp. 1–18, https://doi.org/10.1029/2020jc016551, 2020.

Cazenave, A., Meyssignac, B., Ablain, M., Balmaseda, M., Bamber, J., and Contributors, A.: Global sea-level budget 1993 – present, Earth
  System Science Data, 10, 1551–1590, https://doi.org/https://doi.org/10.5194/essd-10-1551-2018, 2018.

Chambers, D. P., Tamisiea, M. E., Nerem, R. S., and Ries, J. C.: Effects of ice melting on GRACE observations of ocean mass trends,
  Geophysical Research Letters, 34, https://doi.org/https://doi.org/10.1029/2006GL029171, 2007.

Church, J. A. and White, N. J.: A 20th century acceleration in global sea-level rise, Geophysical Research Letters, 33,
  https://doi.org/https://doi.org/10.1029/2005GL024826, 2006.

Consortium, R.: Randolph Glacier Inventory – A Dataset of Global Glacier Outlines: Version 6.0: Technical Report, Global Land Ice Mea-
  surements from Space, Colorado, USA, https://doi.org/https://doi.org/10.7265/N5-RGI-60, 2017.

Crameri, F.: Scientific colour maps., Zenodo, https://doi.org/http://doi.org/10.5281/zenodo.1243862, 2018.

Dziewonski, A. and Anderson, D.: Preliminary reference Earth model, Phys. Earth Plan. Int., 25, https://doi.org/doi:10.17611/DP/9991844,
  1981.

Döll, P., Kaspar, F., and Lehner, B.: A global hydrological model for deriving water availability indicators: model tuning and validation, Journal of Hydrology, 260, 105–134, https://doi.org/https://doi.org/10.1016/S0022-1694(02)00283-4, 2003.

490 Farrell, W. E. and Clark, J. A.: On Postglacial Sea Level, Geophysical Journal of the Royal Astronomical Society, 46, 647–667, 1976.

Fox-Kemper, B., Hewitt, H. T., Xiao, C., Aðalgeirsdóttir, G., Drijfhout, S. S., Edwards, T. L., N. R. Golledge, M. H., Kopp, R. E., Krinner, G., Mix, A., Notz, D., Nowicki, S., Nurhati, I. S., Ruiz, L., Sallée, J.-B., Slangen, A. B. A., and Yu, Y.: Ocean, Cryosphere and Sea Level Change, in: Climate Change 2021: The Physical Science Basis. Contribution of Working Group I to the Sixth Assessment Report of the Intergovernmental Panel on Climate Change, Cambridge University Press, https://www.ipcc.ch/report/ar6/wg1/downloads/report/IPCC_

495   AR6_WGI_Chapter_09.pdf, 2021.

Frederikse, T., Riva, R., Slobbe, C., Broerse, T., and Verlaan, M.: Estimating decadal variability in sea level from tide gauge records: An application to the North Sea, Journal of Geophysical Research: Oceans, 121, 1529–1545, https://doi.org/https://doi.org/10.1002/2015JC011174, 2016.

Frederikse, T., Landerer, F., and Caron, L.: The imprints of contemporary mass redistribution on local sea level and vertical land motion

500   observations, Solid Earth, 10, 1971–1987, https://doi.org/10.5194/se-10-1971-2019, 2019.

Frederikse, T., Landerer, F., Caron, L., Adhikari, S., Parkes, D., Humphrey, V. W., Dangendorf, S., Hogarth, P., Zanna, L., Cheng, L., and Wu, Y. H.: The causes of sea-level rise since 1900, Nature, 584, 393–397, https://doi.org/10.1038/s41586-020-2591-3, 2020.

Gomez, N., Mitrovica, J. X., Tamisiea, M. E., and Clark, P. U.: A new projection of sea level change in response to collapse of marine sectors of the Antarctic Ice Sheet, Geophys. J. Int., 180, 623–634, https://doi.org/10.1111/j.1365-246X.2009.04419.x, 2010.

505 Gregory, J. M., Griffies, S. M., Hughes, C. W., Lowe, J. A., Church, J. A., Fukimori, I., Gomez, N., Kopp, R. E., Landerer, F., Cozannet, G. L., Ponte, R. M., Stammer, D., Tamisiea, M. E., and van de Wal, R. S.: Concepts and Terminology for Sea Level: Mean, Variability and Change, Both Local and Global, Surveys in Geophysics, 40, 1251–1289, https://doi.org/10.1007/s10712-019-09525-z, 2019.

Hamlington, B. D., Reager, J. T., Lo, M. H., Karnauskas, K. B., and Leben, R. R.: Separating decadal global water cycle variability from sea level rise, Scientific Reports, 7, 995, https://doi.org/10.1038/s41598-017-00875-5, 2017.

510 He, X., Bos, M. S., Montillet, J. P., and Fernandes, R. M. S.: Investigation of the noise properties at low frequencies in long GNSS time series, Journal of Geodesy, 93, 1271–1282, https://doi.org/10.1007/s00190-019-01244-y, 2019.

Heij, C., de Boer, P., Franses, P., Kloek, T., and van Dijk, H.: Econometric methods with applications in business and economics, 2004.

Horwath, M., Gutknecht, B. D., Cazenave, A., Palanisamy, H. K., Marti, F., Marzeion, B., Paul, F., Le Bris, R., Hogg, A. E., Otosaka, I., Shepherd, A., Döll, P., Cáceres, D., Müller Schmied, H., Johannessen, J. A., Nilsen, J. E. Ø., Raj, R. P., Forsberg, R., Sandberg Sørensen,

515   L., Barletta, V. R., Simonsen, S. B., Knudsen, P., Andersen, O. B., Randall, H., Rose, S. K., Merchant, C. J., Macintosh, C. R., von Schuckmann, K., Novotny, K., Groh, A., Restano, M., and Benveniste, J.: Global sea-level budget and ocean-mass budget, with focus on advanced data products and uncertainty characterisation, Earth System Science Data Discussions, 2021, 1–51, https://doi.org/10.5194/essd-2021-137, 2021.

Hsu, C. W. and Velicogna, I.: Detection of sea level fingerprints derived from GRACE gravity data, Geophysical Research Letters, 44,

520   8953–8961, https://doi.org/10.1002/2017GL074070, 2017.

Hughes, C. W. and Williams, S. D.: The color of sea level: Importance of spatial variations in spectral shape for assessing the significance of trends, Journal of Geophysical Research: Oceans, 115, https://doi.org/http://dx.doi.org/10.1029/2010JC006102, doi:10.102, 2010.

Jeon, T., Seo, K. W., Kim, B. H., Kim, J. S., Chen, J., and Wilson, C. R.: Sea level fingerprints and regional sea level change, Earth and Planetary Science Letters, 567, 116 985, https://doi.org/10.1016/j.epsl.2021.116985, 2021.

525   Jevrejeva, S., Frederikse, T., Kopp, R. E., Le Cozannet, G., Jackson, L. P., and van de Wal, R. S. W.: Probabilistic Sea Level Projections at the Coast by 2100, Surveys in Geophysics, 40, 1673–1696, 2019.

Landerer, F. W., Flechtner, F. M., Save, H., Webb, F. H., Bandikova, T., Bertiger, W. I., Bettadpur, S. V., Byun, S. H., Dahle, C., Dobslaw, H., Fahnestock, E., Harvey, N., Kang, Z., Kruizinga, G. L., Loomis, B. D., McCullough, C., Murböck, M., Nagel, P., Paik, M., Pie, N., Poole, S., Strekalov, D., Tamisiea, M. E., Wang, F., Watkins, M. M., Wen, H. Y., Wiese, D. N., and Yuan, D. N.: Extending the Global
530   Mass Change Data Record: GRACE Follow-On Instrument and Science Data Performance, Geophysical Research Letters, 47, 1–10, https://doi.org/10.1029/2020GL088306, 2020.

Lange, S.: WFDE5 over land merged with ERA5 over the ocean (W5E5). V. 1.0, GFZ Data Services, https://doi.org/https://doi.org/10.5880/pik.2019.023, 2019.

Larour, E., Ivins, E. R., and Adhikari, S.: Should coastal planners have concern over where land ice is melting?, Science Advances, 3, 1–9,
535   https://doi.org/10.1126/sciadv.1700537, 2017.

Larour, E., Caron, L., Morlighem, M., Adhikari, S., Frederikse, T., Schlegel, N.-J., Ivins, E., Hamlington, B., Kopp, R., and Nowicki, S.: ISSM-SLPS: geodetically compliant Sea-Level Projection System for the Ice-sheet and Sea-level System Model v4.17, Geoscientific Model Development, 13, 4925–4941, https://doi.org/10.5194/gmd-13-4925-2020, 2020.

Lehner, B., Liermann, C. R., Revenga, C., Vörösmarty, C., Fekete, B., Crouzet, P., Döll, P., Endejan, M., Frenken, K., Magome, J., Nilsson,
540   C., Robertson, J. C., Rödel, R., Sindorf, N., and Wisser, D.: High-resolution mapping of the world's reservoirs and dams for sustainable river-flow management, Frontiers in Ecology and the Environment, 9, 494–502, https://doi.org/https://doi.org/10.1890/100125, 2011.

Lin, Y., Hibbert, F. D., Whitehouse, P. L., Woodroffe, S. A., Purcell, A., Shennan, I., and Bradley, S. L.: A reconciled solution of Meltwater Pulse 1A sources using sea-level fingerprinting, Nature Communications, 12, 2015, https://doi.org/10.1038/s41467-021-21990-y, 2021.

MacIntosh, C. R., Merchant, C. J., and von Schuckmann, K.: Uncertainties in Steric Sea Level Change Estimation During the Satellite
545   Altimeter Era: Concepts and Practices, Surveys in Geophysics, 38, 59–87, 2017.

Marzeion, B., Jarosch, A. H., and Hofer, M.: Past and future sea-level change from the surface mass balance of glaciers, Cryosphere, 6, 1295–1322, https://doi.org/10.5194/tc-6-1295-2012, 2012.

Milne, G. A. and Mitrovica, J. X.: Postglacial sea-level change on a rotating Earth, Geophysical Journal International, 133, 1–19, https://doi.org/https://doi.org/10.1046/j.1365-246X.1998.1331455.x, 1998.

550   Mitrovica, J., Tamisiea, M., Davis, J., and Milne, G.: Recent mass balance of polar ice sheets inferred from patterns of global sea-level change, Nature, 409, 1026–1029, https://doi.org/10.1038/35059054, 2001.

Mitrovica, J., Gomez, N., Morrow, E., Hay, C., Latychev, K., and Tamisiea, M.: On the robustness of predictions of sea level fingerprints, Geophysical Journal International, 187, 729–742, https://doi.org/10.1111/j.1365-246X.2011.05090.x, 2011.

Mitrovica, J. X. and Peltier, W. R.: On Postglacial Geoid Subsidence Over the Equatorial Oceans, Journal of Geophysical Research, 96,
555   20 053–20 071, https://doi.org/https://doi.org/10.1029/91JB01284, 1991.

Mouginot, J. and Rignot, E.: Glacier Catchments/Basins for the Greenland Ice Sheet, Dryad, https://doi.org/doi:10.7280/D1WT11, 2019.

Mouginot, J., Rignot, E., Bjørk, A. A., van den Broeke, M., Millan, R., Morlighem, M., Noël, B., Scheuchl, B., and Wood, M.: Supplement of Forty-six years of Greenland Ice Sheet mass balance from 1972 to 2018, Proceedings of the National Academy of Sciences of the United States of America, 116, 9239–9244, https://doi.org/10.1073/pnas.1904242116, 2019.

560   Nerem, R. S., Beckley, B. D., Fasullo, J. T., Hamlington, B. D., Masters, D., and Mitchum, G. T.: Climate-change–driven accelerated sea-level rise detected in the altimeter era, Proceedings of the National Academy of Sciences, 115, 2022–2025, https://doi.org/10.1073/pnas.1717312115, 2018.

Nicholls, R., Wong, P., Burkett, V., Codignotto, J., Hay, J., McLean, R., Ragoonaden, S., and Woodroffe, C.: Coastal systems and low-lying areas, in: Climate Change 2007: Impacts, Adaptation and Vulnerability. Contribution of Working Group II to the Fourth Assessment Report of the Intergovernmental Panel on Climate Change, Cambridge University Press, https://doi.org/https://ro.uow.edu.au/scipapers/164, 2007.

Oppenheimer, M., Abdelgawad, A., Hay, J., Glavovic, B., Cai, R., Marzeion, B., Hinkel, J., Cifuentes-Jara, M., Meyssignac, B., Van De Wal, R., DeConto, R., Sebesvari, Z., Magnan, A., and Ghosh, T.: Sea Level Rise and Implications for Low-Lying Islands, Coasts and Communities, in: IPCC Special Report on the Ocean and Cryosphere in a Changing Climate, pp. 76–95, In press., https://report.ipcc.ch/srocc/pdf/SROCC{_}FinalDraft{_}Chapter4.pdf, 2019.

Palmer, M. D., Domingues, C. M., Slangen, A. B. A., and Boeira Dias, F.: An ensemble approach to quantify global mean sea-level rise over the 20th century from tide gauge reconstructions, Environmental Research Letters, 16, 044 043, https://doi.org/10.1088/1748-9326/abdaec, 2021.

Peltier, W. R., Argus, D. F., and Drummond, R.: Comment on "An Assessment of the ICE-6G_C (VM5a) Glacial Isostatic Adjustment Model" by Purcell et al., Journal of Geophysical Research: Solid Earth, 123, 2019–2028, https://doi.org/10.1002/2016JB013844, 2018.

Pfeffer, W. T., Arendt, A. A., Bliss, A., Bolch, T., Cogley, J. G., Gardner, A. S., Hagen, J.-O., Hock, R., Kaser, G., Kienholz, C., and et al.: The Randolph Glacier Inventory: a globally complete inventory of glaciers, Journal of Glaciology, 60, 537–552, https://doi.org/10.3189/2014JoG13J176, 2014.

Prandi, P., Meyssignac, B., Ablain, M., Spada, G., Ribes, A., and Benveniste, J.: Local sea level trends, accelerations and uncertainties over 1993–2019, Scientific Data, 8, 1–12, https://doi.org/10.1038/s41597-020-00786-7, 2021.

Rignot, E., Mouginot, J., and Scheuchl, B.: Antarctic grounding line mapping from differential satellite radar interferometry, Geophysical Research Letters, 38, https://doi.org/https://doi.org/10.1029/2011GL047109, 2011.

Rignot, E., Mouginot, J., Scheuchl, B., Van Den Broeke, M., Van Wessem, M. J., and Morlighem, M.: Four decades of Antarctic ice sheet mass balance from 1979–2017, Proceedings of the National Academy of Sciences of the United States of America, 116, 1095–1103, https://doi.org/10.1073/pnas.1812883116, 2019.

Riva, R., Bamber, J., Lavallee, D., and Wouters, B.: Sea-level fingerprint of continental water and ice mass change from GRACE, Geophysical Research Letters, 37, 1–6, https://doi.org/10.1029/2010GL044770, 2010.

Royston, S., Watson, C. S., Legrésy, B., King, M. A., Church, J. A., and Bos, M. S.: Sea-Level Trend Uncertainty With Pacific Climatic Variability and Temporally-Correlated Noise, Journal of Geophysical Research: Oceans, 123, 1978–1993, https://doi.org/https://doi.org/10.1002/2017JC013655, 2018.

Save, H.: CSR GRACE and GRACE-FO RL06 Mascon Solutions v02, CSR, https://doi.org/doi: 10.15781/cgq9-nh24, 2020.

Save, H., Bettadpur, S., and Tapley, B. D.: High-resolution CSR GRACE RL05 mascons, Journal of Geophysical Research : Solid Earth, 121, 7547–7569, https://doi.org/10.1002/2017JB015312, 2016.

Schneider, U., Becker, A., Finger, P., Meyer-Christoffer, A., Rudolf, B., and Ziese, M.: GPCC full data reanalysis version 7.0 at 0.5◦: monthly land-surface precipitation from rain-gauges built on GTS-based and historic data, Global Precipitation Climatology Centre (GPCC, http://gpcc.dwd.de/, https://doi.org/https://doi.org/10.5676/dwd_gpcc/fd_m_v7_050, 2015, 2015.

Schwarz, G.: Estimating the Dimension of a Model, The Annals of Statistics, 6, 461–464, 1978.

Shepherd, A., Ivins, E., Rignot, E., Smith, B., Van Den Broeke, M., Velicogna, I., Whitehouse, P., Briggs, K., Joughin, I., Krinner, G., Nowicki, S., Payne, T., Scambos, T., Schlegel, N., Geruo, A., Agosta, C., Ahlstrøm, A., Babonis, G., Barletta, V., Blazquez, A., Bonin, J., Csatho, B., Cullather, R., Felikson, D., Fettweis, X., Forsberg, R., Gallee, H., Gardner, A., Gilbert, L., Groh, A., Gunter, B., Hanna, E., Harig, C., Helm, V., Horvath, A., Horwath, M., Khan, S., Kjeldsen, K. K., Konrad, H., Langen, P., Lecavalier, B., Loomis, B., Luthcke, S.,

McMillan, M., Melini, D., Mernild, S., Mohajerani, Y., Moore, P., Mouginot, J., Moyano, G., Muir, A., Nagler, T., Nield, G., Nilsson, J., Noel, B., Otosaka, I., Pattle, M. E., Peltier, W. R., Pie, N., Rietbroek, R., Rott, H., Sandberg-Sørensen, L., Sasgen, I., Save, H., Scheuchl, B., Schrama, E., Schröder, L., Seo, K. W., Simonsen, S., Slater, T., Spada, G., Sutterley, T., Talpe, M., Tarasov, L., Van De Berg, W. J., Van Der Wal, W., Van Wessem, M., Vishwakarma, B. D., Wiese, D., and Wouters, B.: Mass balance of the Antarctic Ice Sheet from 1992 to 2017, Nature, 558, 219–222, https://doi.org/10.1038/s41586-018-0179-y, 2018.

Shepherd, A., Ivins, E., Rignot, E., Smith, B., van den Broeke, M., Velicogna, I., Whitehouse, P., Briggs, K., Joughin, I., Krinner, G., Nowicki, S., Payne, T., Scambos, T., Schlegel, N., A, G., Agosta, C., Ahlstrøm, A., Babonis, G., Barletta, V. R., Bjørk, A. A., Blazquez, A., Bonin, J., Colgan, W., Csatho, B., Cullather, R., Engdahl, M. E., Felikson, D., Fettweis, X., Forsberg, R., Hogg, A. E., Gallee, H., Gardner, A., Gilbert, L., Gourmelen, N., Groh, A., Gunter, B., Hanna, E., Harig, C., Helm, V., Horvath, A., Horwath, M., Khan, S., Kjeldsen, K. K., Konrad, H., Langen, P. L., Lecavalier, B., Loomis, B., Luthcke, S., McMillan, M., Melini, D., Mernild, S., Mohajerani, Y., Moore, P., Mottram, R., Mouginot, J., Moyano, G., Muir, A., Nagler, T., Nield, G., Nilsson, J., Noël, B., Otosaka, I., Pattle, M. E., Peltier, W. R., Pie, N., Rietbroek, R., Rott, H., Sandberg Sørensen, L., Sasgen, I., Save, H., Scheuchl, B., Schrama, E., Schröder, L., Seo, K. W., Simonsen, S. B., Slater, T., Spada, G., Sutterley, T., Talpe, M., Tarasov, L., van de Berg, W. J., van der Wal, W., van Wessem, M., Vishwakarma, B. D., Wiese, D., Wilton, D., Wagner, T., Wouters, B., and Wuite, J.: Mass balance of the Greenland Ice Sheet from 1992 to 2018, Nature, 579, 233–239, https://doi.org/10.1038/s41586-019-1855-2, 2020.

Slangen, A. B. A., Katsman, C. A., van de Wal, R. S. W., Vermeersen, L. L. A., and Riva, R. E. M.: Towards regional projections of twenty-first century sea-level change based on IPCC SRES scenarios, Climate Dynamics, 38, 1191–1209, 2012.

Slangen, A. B. A., van de Wal, R. S. W., Wada, Y., and Vermeersen, L. L. A.: Comparing tide gauge observations to regional patterns of sea-level change (1961-2003), Earth System Dynamics, 5, 243–255, https://doi.org/10.5194/esd-5-243-2014, 2014.

Sutanudjaja, E. H., Van Beek, R., Wanders, N., Wada, Y., Bosmans, J. H., Drost, N., Van Der Ent, R. J., De Graaf, I. E., Hoch, J. M., De Jong, K., Karssenberg, D., López López, P., Peßenteiner, S., Schmitz, O., Straatsma, M. W., Vannametee, E., Wisser, D., and Bierkens, M. F.: PCR-GLOBWB 2: A 5 arcmin global hydrological and water resources model, Geoscientific Model Development, 11, 2429–2453, https://doi.org/10.5194/gmd-11-2429-2018, 2018.

Tamisiea, M. E. and Mitrovica, J. X.: The Moving boundaries of Sea Level Change, Oceanography, 24, 24–39, https://doi.org/10.5670/oceanog.2011.25.COPYRIGHT, 2011.

Tapley, B. D., Bettadpur, S., Watkins, M., and Reigber, C.: The Gravity Recovery and Climate Experiment: Mission Overview and Early Results, AGU, 2004.

Thorne, P.: Global surface temperatures, in: Climate Change, pp. 95–109, Elsevier B.V., https://doi.org/10.1016/b978-0-12-821575-3.00005-0, 2021.

Thorne, P., Parkes, D., Christy, J., and Mears, C.: Lessons from Upper-Air Temperature Records, American Meteorological Society, 86, 1437–1442, https://doi.org/10.1175/BAMS-86-I0-I437, 2005.

Vishwakarma, B. D., Bates, P., Sneeuw, N., Westaway, R. M., and Bamber, J. L.: Re-assessing global water storage trends from GRACE time series, Environmental Research Letters, 16, 034 005, https://doi.org/10.1088/1748-9326/abd4a9, 2021.

Wahr, J., Swenson, S., and Velicogna, I.: Accuracy of GRACE mass estimates, Geophysical Research Letters, 33, https://doi.org/https://doi.org/10.1029/2005GL025305, 2006.

Watkins, M. M., Wiese, D. N., Yuan, D.-N., Boening, C., and Landerer, F. W.: Improved methods for observing Earth's time variable mass distribution with GRACE using spherical cap mascons, JGR: Solid Earth, 120, 1648–2671, https://doi.org/10.1002/2014JB011547, 2015.

WCRP, G. S. L. B. G.: Global sea-level budget 1993–present, Earth System Science Data, 10, 1551–1590, https://doi.org/10.5194/essd-10-1551-2018, 2018.

640 Weedon, G. P., Balsamo, G., Bellouin, N., Gomes, S., Best, M. J., and Viterbo, P.: The WFDEI meteorological forcing data set: WATCH Forcing Data methodology applied to ERA-Interim reanalysis data, Water Resources Research, 50, 7505–7514, https://doi.org/https://doi.org/10.1002/2014WR015638, 2014.

WGMS: Fluctuations of Glaciers Database, World Glacier Monitoring Service, Zurich, Switzerland, https://doi.org/10.5904/wgms-fog-2021-05, 2021.

645 Wiese, D. N., Landerer, F. W., and Watkins, M. M.: Quantifying and reducing leakage errors in the JPL RL05M GRACE mascon solution, Water Resources Research, 52, https://doi.org/doi:10.1002/2016WR019344, 2016.

Wiese, D. N., Yuan, D.-N., Boening, C., Landerer, F. W., and M., W. M.: JPL GRACE Mascon Ocean, Ice, and Hydrology Equivalent Water Height RL06 CRI Filtered Version 02. Ver. 02. PO.DAAC, CA, USA., JPL, Dataset accessed [2020-10-28], https://doi.org/https://doi.org/10.5067/TEMSC-3JC62, 2019.

650 Wigley, T. M. L.: The Climate Change Commitment, Science, 307, 1766–1769, https://doi.org/10.1126/science.1103934, 2005.

Zemp, M., Huss, M., Thibert, E., Eckert, N., McNabb, R., Huber, J., Barandun, M., Machguth, H., Nussbaumer, S. U., Gärtner-Roer, I., Thomson, L., Paul, F., Maussion, F., Kutuzov, S., and Cogley, J. G.: Global glacier mass changes and their contributions to sea-level rise from 1961 to 2016, Nature, 568, 382–386, https://doi.org/10.1038/s41586-019-1071-0, 2019.